GCAGS JOURNAL
A Publication of the Gulf Coast Association of Geological Societies
www.gcags.org

Spectrum of Nanopores, Micropores, and Associated Pore Networks and their Origins in Carbonate Strata

Robert G. Loucks

Bureau of Economic Geology, Jackson School of Geosciences,
The University of Texas at Austin, Austin, Texas, U.S.A.

ABSTRACT

Nano- and micropores (defined as pores less than 10 µm in diameter) are common in carbonate reservoirs as either the sole pore type or in combination (dual pore networks) with matrix macropores and fracture pores. These very fine-scale pores form in limestones and dolostones and in associated organic matter (e.g., solid bitumen). Limestone nano- and micropores occur between crystals that are commonly less than 1 to 9 µm in size in limestone, but in dolostone the crystal size can be much larger. Limestone nano- and micropores commonly originate in three ways, although some inherited original nano- and micropores between mud components are preserved.

First, in original lime-mud mixtures of aragonite, Mg–calcite, and calcite, the origin is both depositional and diagenetic as aragonite dissolves and reprecipitates because microrhombic calcite, Mg–calcite transforms to microrhombic calcite, and original calcite grains are generally unaffected. Second, in chalks, nano-and micropores are related to the original depositional fabric as interparticle pores between coccoliths and other pelagic allochems. Third, in sediment originally composed of Mg–calcite-rich allochems, nano-and micropores form by transformation of unstable Mg–calcite allochems to microrhombic calcite.

In dolostones, nano-and micropores are associated with extensive dolomitization and the nearly complete occlusion of pores (overdolomitization), whereas another diagenetic origin in dolostones is differential dolomitization at the grain scale. Also, in some dolostones, nano- to micropores pores are inherited from precursor microporous limestone.

A late process of nano- and micropore formation is subaerial weathering of both limestones and dolostones resulting in pulverulite. This form of micropores is commonly developed at unconformities as enhanced porosity zones.

Organic-matter nano- and micropores in solid bitumen, common in thermally mature organic-rich argillaceous limestone, can also be present in coarser-grained carbonates in which solid-bitumen occurs within macropores. Only in organic-rich limestones do organic-matter pores have potential to form an effective pore system.

Because nano- and micropores have multiple origins, their lateral and vertical distribution reflects or depends on their origin; therefore, one must not only describe nano- and micropores, but also define their origin. Recognition of nano- and micropores is important because they form tight carbonate reservoirs and have significant effects on permeability, porosity perseveration with burial, hydrocarbon saturation, hydrocarbon recovery, sweep efficiency, storage, and reserve estimations. Not recognizing nano- and micropore networks can lead to errors relative to the aforementioned measurements and as a result, economic evaluations may be invalid.

INTRODUCTION

Pores associated with carbonate strata range from nano- to cavernous pores (Choquette and Pray, 1970). Mesopores and megapores (≥10 µm) (Fig. 1) are easily recognized and are generally well described; however, nano- and micropores (<10 µm) (Fig. 1) commonly are not recognized because of their very fine size and therefore advanced analytical techniques are necessary for characterizeng their properties. A number of researchers (e.g., Pittman [1971], Handford et al. [1989], Moshier [1989], Deville de Periere et al. [2011], Loucks et al. [2012], Kaczmarek et al. [2015], Loucks [2017], Hashim and Kaczmarek [2019], and Janjuhah et al. [2019]) have described and classified these nano- and micropores; however, researchers have rarely addressed the origin of the nano- and micropores or addressed nano- and micropores in dolostones.

Nano- and micropores, very common in carbonates, can have significant effects on reservoir and petrophysical properties (e.g., Eberli et al. [2003], Vanorio and Mavko [2009], Zahm and Enderlin [2010], Deville de Periere et al. [2011], Loucks et al. [2012], Kaczmarek et al. [2015], Janjuhah et al. [2019], and Liu et al. [2021]). The pores occur in limestones and dolomites as well as in organic matter (generally solid bitumen) within carbonate pores. The origin of nano- and micropores is quite varia-

Manuscript received July 3, 2024; revised manuscript received August 19, 2024; manuscript accepted August 19, 2024.

GCAGS Journal, v. 13 (2024), p. 75–109.
https://doi.org/10.62371/ZOPM1581

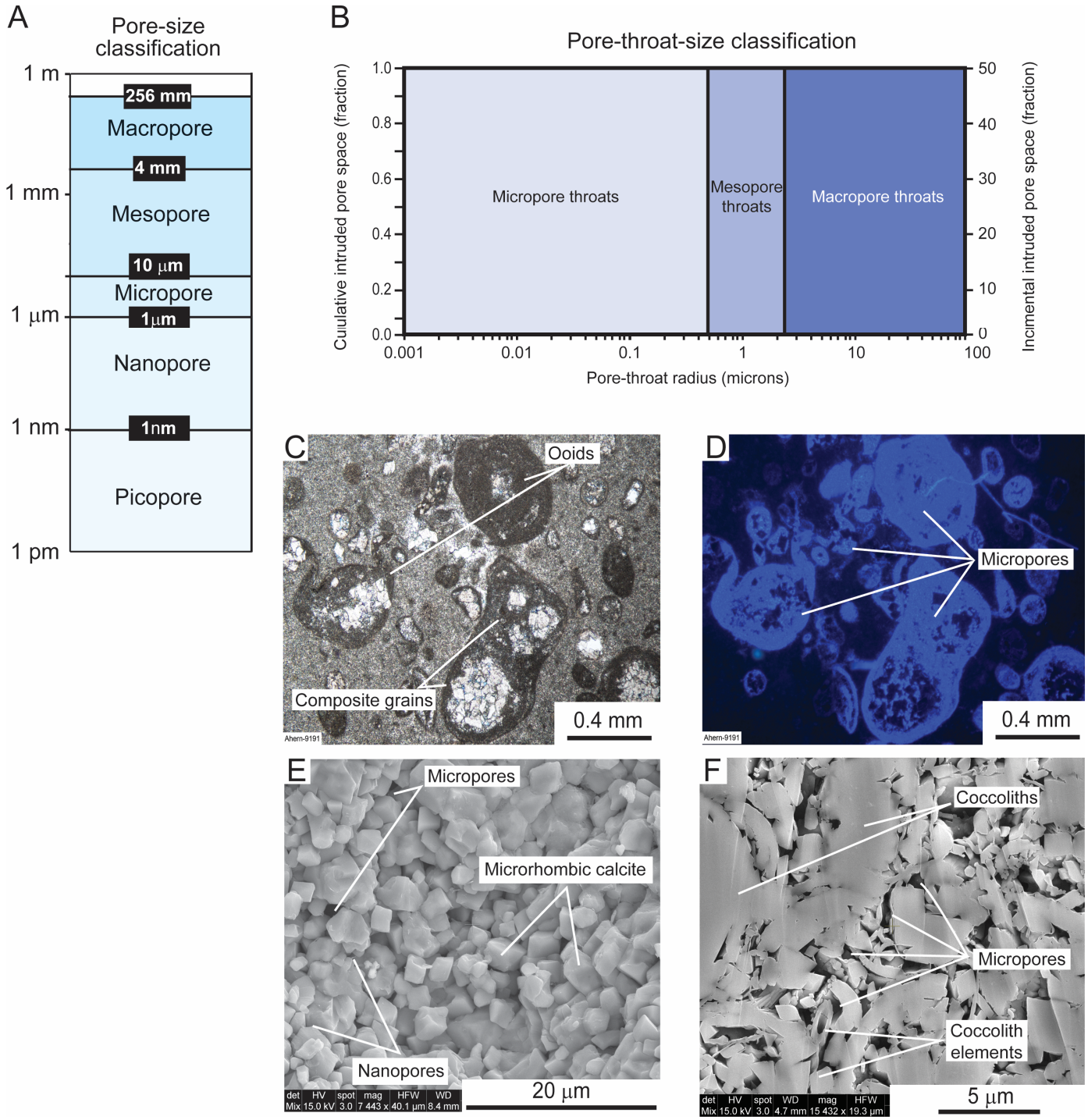

Figure 1. Nano- and micropore-size classifications and examples. (A) Pore-size classification emphasizing range from picopore to macropore (modified after Loucks et al. [2012]). (B) Pore-size classification of pore throats. Image slightly modified from a Core Laboratories report. (C) Thin-section photomicrograph of *Komia* grainstone from Pennsylvanian Caddo Formation in north-central Texas. (D) Same thin section as in C but under UV light. Distribution of micropores shown in blue. (E) Scanning electron microscope (SEM) image of rock chip from Lower Cretaceous Calvin Formation in northern Louisiana. Sample composed of microrhombic calcite and associated nano- and micropores. (F) SEM image (Ar–ion-milled sample) from upper Annona Chalk in northwestern Louisiana. Sample displays abundant nano- and micropores. Grains include coccolith plates and disaggregated coccolith elements.

ble, ranging from depositional to diagenetic, and the spatial distribution of these pores is commonly related to their origin. Recognition of nano- and micropores is important as they form tight carbonate reservoirs and commonly form a substantial portion of the pore network in many carbonate reservoirs (i.e., dual pore networks). Nano- and micropores also, have significant effects on permeability, hydrocarbon saturation, seismic attributes, rock strength, hydrocarbon recovery, sweep efficiency, storage, and reserve estimations; therefore, these pore types need to be quantified and their distribution documented in order to define

many economic factors such as reservoir quality, fluid saturations, reservoir recovery, and reserve estimations.

The overall goal of this review is to outline the broad spectrum of nano- and micropore pore types and their origins. Specific objectives are to: (1) clarify the definition of nano- and micropores and associated pore networks, (2) survey the broad spectrum of nano- and micropores in limestones, dolostones, and organic matter in carbonates, (3) discuss probable origins of different nano- and micropore types, (4) review methods on how to recognize and quantify nano- and micropores, (5) speculate on the spatial distribution of nano- and micropore types based on their origin, and (6) discuss the effects of nano- and micropores on reservoir quality, pore preservation with burial, seismic attributes, rock strength, hydrocarbon saturation, hydrocarbon recovery, sweep efficiency, storage, and reserve estimates. This study will provide the information necessary for recognizing and understanding these nano- and micropore types and their effects on carbonate reservoirs.

DATA

Data for this review come from the literature and from extensive research by the author on strata from many ages and from a worldwide distribution. In addition to numerous case studies by the author, a number of case studies from the literature have been reviewed (e.g., Cantrell and Hagerty [1999], Deville de Periere et al. [2011], and Yamamoto et al. [2011]). Some of the concepts presented in this review have been previously published by the author or other authors. Some new concepts by the author, especially relative to dolostones and organic matter in carbonates, will also be discussed. Pittman (1971) was one of the first to draw attention to what micropores are and some of the effects that micropores have on petrophysical properties. Microrhombic calcite and associated micropores were later discussed in depth at the 1987 Society of Economic Paleontologists and Mineralogists Midyear Meeting in Austin, Texas, in a technical session, "Reservoir Diagenesis and the Evolution of Micro- and Macro-Pore Networks in Carbonate Rocks," convened and chaired by R. G. Loucks and C. R. Handford. A special volume of *Sedimentary Geology* (Handford et al., 1989) published two years later contained 11 papers from this session. Since then, many authors have attempted to define the origin of microrhombic calcite and associated micropores, and the suggested origins vary greatly (e.g., see papers in Handford et al. [1989] and Kaczmarek et al. [2015]). Kaczmarek et al. (2015) advanced our understanding of the characteristics of micropores when they presented a universal classification scheme for the microcrystals that host limestone micropores. Note that some authors (e.g., Kaczmarek et al. [2015]) use the term *microporosity* for *micropores*. Porosity is a measure of pore volume and should not be used to describe actual pores. However, the term *microporous* can be used because it defines a porous rock that contains abundant nano- and micropores.

Several thousand thin sections have been analyzed by the present author and each thin section was impregnated with (1) blue-dyed epoxy to emphasize macropores and (2) fluorescent, blue-dyed epoxy to identify nano- and micropores (Figs. 1C and 1D). The thin sections were viewed with a petrographic microscope using a reflective ultraviolet (UV) light source to activate the fluorescent, blue-dyed epoxy. Actual individual nano- and micropores are not well imaged using fluorescent blue dye but the resulting blue haze indicates areas of nano- and micropores (e.g., Figures 2B and 2G).

Scanning electron microscopy (SEM) was used to image nano- and micropores. Rock chips were used to image the three-dimensional form of the microcrystals and associated nano- to micropores (e.g., Figure 1E). Ar–ion milled samples (see Loucks et al. [2009] for sample preparation description) were prepared to allow imaging of a flat surface to obtain actual two-dimensional pore shapes, dimensions, and distribution (e.g., Figures 1F and 2D). The Ar–ion milling technique provided only a small image area of approximately 0.2 mm by 1 mm; however, with pore sizes being less than a few microns, numerous pores are observable. SEM imaging was conducted on a FEI Nova NanoSEM 430 system at the Bureau of Economic Geology, The University of Texas at Austin. Standard procedures used were an accelerating voltage of 10 to 15 kV with a working distance of 3 to 10 mm. Other techniques used to characterize nano- and micropores are discussed in a later section.

Later in this review are a series of case histories that emphasize different nano- and micropore networks. These case histories present a wide variety of photographs, photomicrographs, and SEM images referred to in the introductory material.

DEFINITION OF NANO- AND MICROPORES

Two different approaches define nano- and micropores in carbonates. One is based on pore size and the other is based on pore-throat size (Figs. 1A and 1B). In this study, *pore size* is used as the definition of nano- and micropores because a pore can be readily viewed and imaged. *Pore-throat size* is a measurement obtained generally from mercury injection capillary pressure (MICP) analysis (Schowalter, 1979).

The first approach is based on dimensions of the pore. A *micropore* is defined as a pore having a long diameter ≥1 μm but <10 μm (Fig. 1A) (e.g., Cantrell and Hagerty [1999] and Loucks et al. [2013]) and these pores are generally viewed using SEM. A *nanopore* is defined as a pore with with a long dimension <1 μm and >1 nm (Fig. 1A). Another micropore classification scheme is based on the pore-throat size that connects pores. If the pore-throat radius between pores is ≤0.5 μm it is considered a micropore (Fig. 1B) (Pittman, 1971). These definitions are similar to definitions proposed by Pittman (1971), Handford et al. (1989), Cantrell and Hagerty (1999), and Loucks et al. (2013). In many limestones with abundant nano- and micropores, pores occur between microcrystalline calcite rhombs ranging in size between 0.5 between 9 μm with a mode of approximately 2 μm (Kaczmarek et al., 2015). In dolostone, crystal sizes can be larger than 9 μm (per this investigation).

Note that nano- and micropores must be considered relative to the whole pore network (Fig. 2) for their effect on reservoir quality and petrophysical characteristics to be understood. Because the pore network can range from homogenous to heterogenous (e.g., Figures 2B and 2G), a nano- to micropore network is one in which nanopore and/or micropore throats connect to form much of the effective pore network, even if macropores are present. Such a situation of macropores being connected by micropores commonly exists in oomoldic grainstones, in which the intraparticle oomoldic pores are separated by relatively cemented interparticle pores with nano- to micropore throats (Fig. 3). As seen in an Upper Jurassic Smackover example from northeastern Texas (Fig. 3), the interparticle pores are nearly filled with calcite cement, whereas the oomoldic pores are generally open. In this case, the nano- and micropore throats between the interparticle calcite crystals produce an effective pore network, resulting in a low-permeability pore system in which the larger oomoldic pores are commonly poorly drained.

Another case in which larger pores dominate the pore volume but nano- to micropore distribution controls the reservoir quality of the rock from the Eocene of offshore Tunisia (Loucks et al., 1998) (Fig. 4). The skeletal grains (large foraminifers, *Nummulites*) that were originally Mg–calcite stabilized to microrhombic calcite and produced associated nano- and micropores. The intraparticle pores in the larger foraminifers are now connected to the effective interparticle pore system through the microporous walls of the foraminifers. Walls of the *Nummulites* tests are composed of micropores (Fig. 4). Because the microporous walls of the *Nummulites* tests control connectivity of

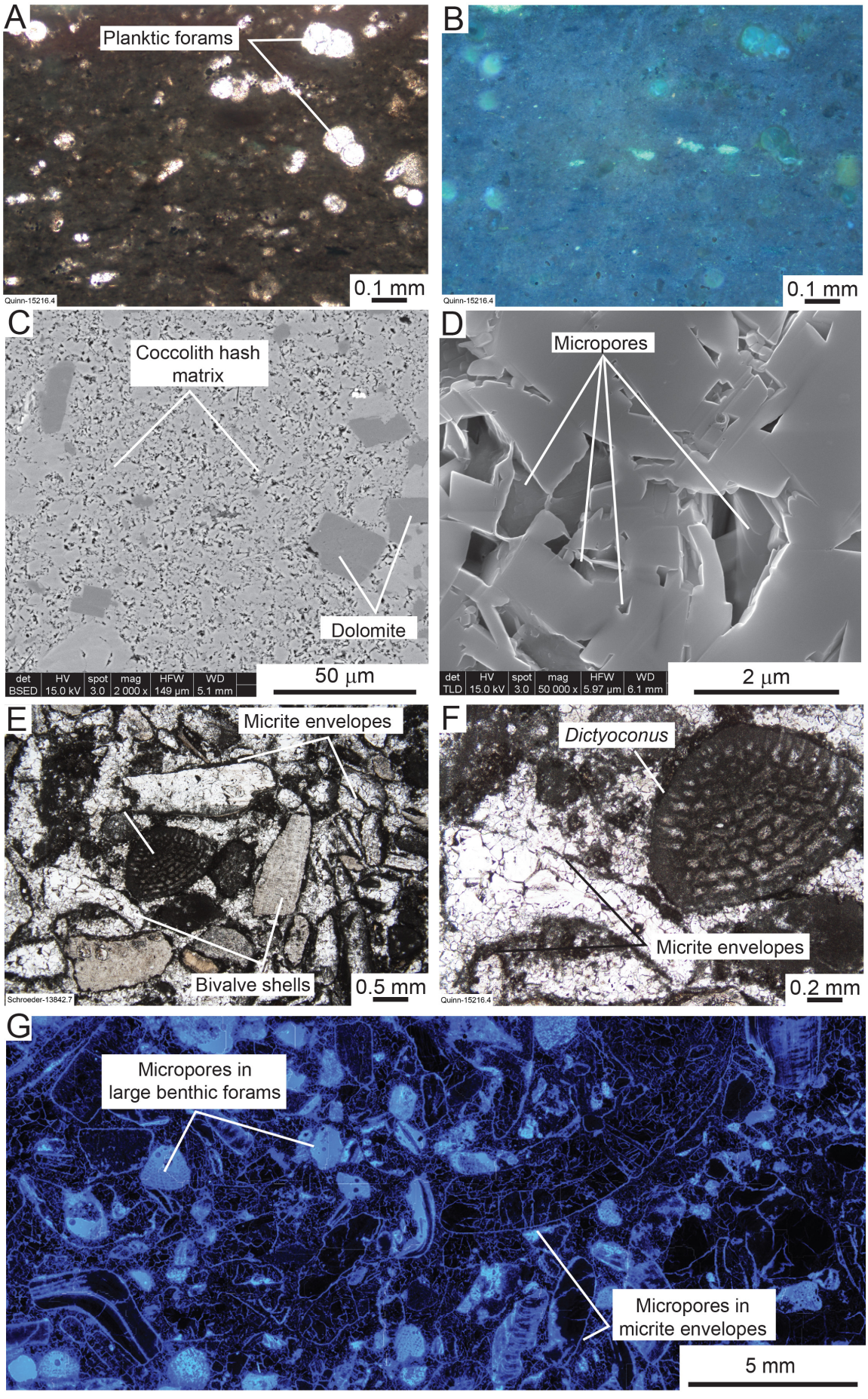
A
Planktic forams
0.1 mm
Quinn-15216.4
B
0.1 mm
Quinn-15216.4
C
Coccolith hash matrix
Dolomite
det HV spot mag HFW WD
BSED 15.0 kV 3.0 2 000 x 149 µm 5.1 mm
50 µm
D
Micropores
det HV spot mag HFW WD
TLD 15.0 kV 3.0 50 000 x 5.97 µm 6.1 mm
2 µm
E
Micrite envelopes
Bivalve shells
0.5 mm
Schroeder-13842.7
F
Dictyoconus
Micrite envelopes
0.2 mm
Quinn-15216.4
G
Micropores in large benthic forams
Micropores in micrite envelopes
5 mm

(FACING PAGE) Figure 2. Examples of nano- to micropore networks. (A) Thin-section photomicrograph of marly chalk wackestone from Louisiana showing planktic foraminifers in peloidal matrix. Upper Cretaceous Austin Chalk Formation, Louisiana. (B) Same as A, but photomicrograph taken under UV light. Microporous coccolith-hash-mud matrix, as indicated by blue haze. Pore network in this example is relatively uniform or homogenous. (C) Same sample as in A. Ar–ion-milled SEM image showing coccolith-hash matrix with associated micropores. Some dolomite crystals are present. (D) Close-up of C showing interparticle nano- and micropores. (E) Thin-section photomicrograph of Lower Cretaceous Stuart City Formation, well-cemented lime grainstone from South Texas. (F) Close-up photomicrograph of E showing larger foraminifer (*Dictyoconus*)—originally Mg–calcite and now composed of microrhombic calcite. (G) Mosaic of photomicrographs under UV light from Lower Cretaceous Stuart City Formation in South Texas. Light blue areas within and around grains are microporous. Example of complex micropore network.

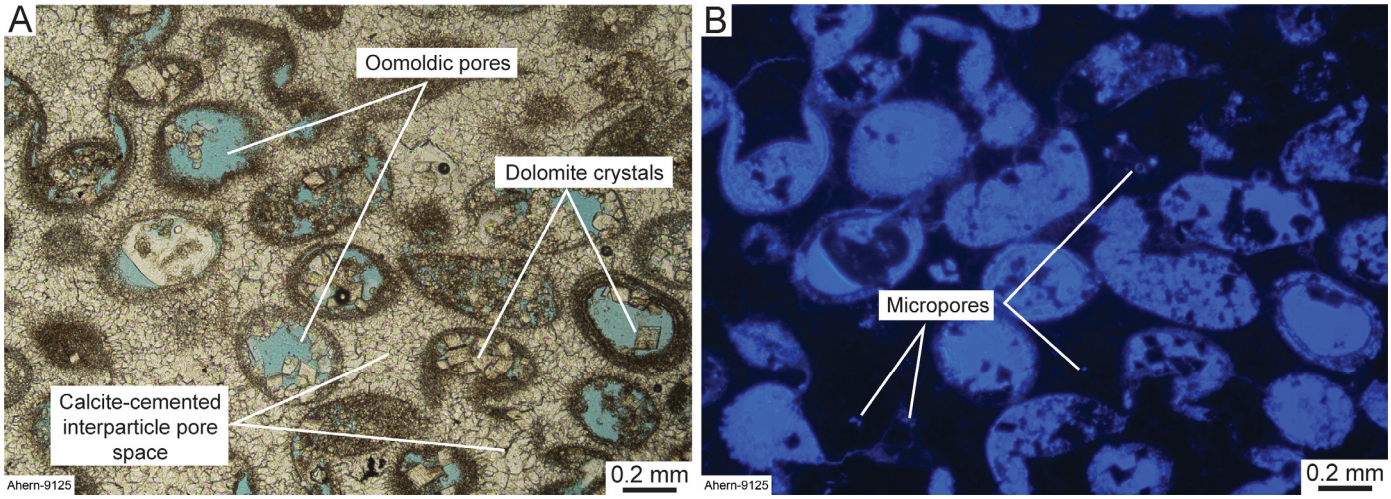

Figure 3. Example of oomoldic pores isolated from each other by micropore network. (A) Thin section of Upper Jurassic Smackover Formation ooid grainstone in northeastern Texas. Ooids are dissolved to form macropores isolated from each other; permeability is controlled by micropore system in cemented interparticle pore space. Porosity = 13.4% and permeability = 0.077 md. (B) Same as A, but photomicrograph taken under ultraviolet (UV) light. Microporous areas are indicated by blue haze.

intraparticle pores within the foraminifers to the effective interparticle pore network in these grainstones, the nano- to micropore network, in turn, has a controlling effect on permeability pathways.

APPROACHES TO IDENTIFYING, IMAGING, AND QUANTIFYING NANO- AND MICROPORES

Special techniques are needed to identify, image, and quantify nano- and micropores, as well as micropore throats. Some techniques are only for imaging, whereas other techniques can be used in imaging and/or quantification. A brief summary of several of the more commonly utilized techniques follows.

Petrographic Thin-Section Analysis

Thin sections are commonly impregnated with blue-dyed epoxy to emphasize macropores (e.g., Figures 3A and 4A), and to highlight nano- and micropores, a blue-fluorescent-dye is added to the epoxy (e.g., Figures 1D and 2G). Thin sections are viewed using a petrographic microscope with a reflecting light source that can excite the fluorescent blue dye and highlight where the dye is present in the finer pore structure of the thin section. Nano- and micropores will generally appear as a blue haze because the individual pores may be too fine to resolve (e.g., Figures 2A and 2B), although in some samples individual micropores can be crudely imaged on a petrographic microscope at 200 to 500× magnification.

A method of quantifying nano- and micropores is point counting thin sections with a petrographic scope and comparing the visible porosity to the measured porosity obtained by conventional core analysis. Generally, measured conventional core porosity is higher than thin-section point-count porosity (Fig. 5). Tthe difference in porosity between the two techniques is attributed to the presence of nano- and micropores not readily visible during point counting. Although this method allows for an estimate of the abundance of nano- and micropores, it should not be taken as an exact value.

Scanning Electron Microscopy (SEM)

The best method of imaging nano- and micropores is by SEM analysis (e.g., Figures 1E and 1F). SEM provides the imaging power necessary to resolve pore sizes down to approximately 3 to 5 nm, and the type of imaging varies by the type of sample prepared. Quantification by SEM analysis of nano- and micropores can best be done on samples prepared by Ar–ion milling or by polished thin sections. Ar–ion-milled samples were first used by Loucks et al. (2009) to image nanopores in organic matter and this technique has become one of the established methods of viewing nano- and micropores. The milling process provides an extremely flat surface that permits the cross-sectional shape of the pores to be imaged and measured (e.g., Figure 1F). Also, some degree of the three-dimensional depth of the pores can be viewed (e.g., Figure 2D). Although images of Ar–ion milled surfaces can be point counted for abundance using programs such as JMicroVision (Roduit, 2008), the area covered is limited.

Rock chips viewed using SEM show the three-dimensional shape of the crystals and associated nano- and micropores (e.g., Figure 1E); however, quantifying pore abundances by this meth-

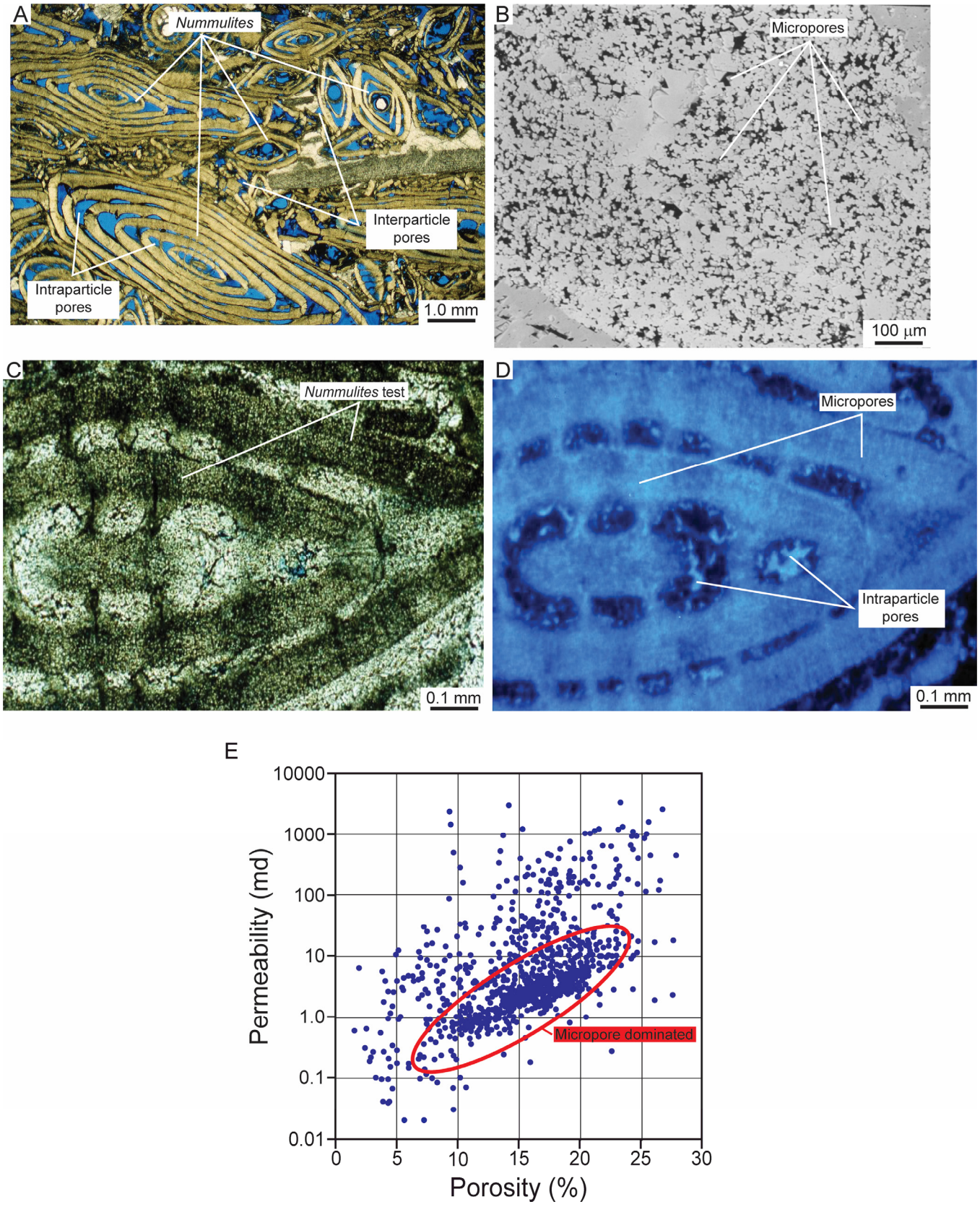

Figure 4. Mg–calcite-dominated microporous rocks. Lower Eocene El Garia Formation, offshore Tunisia. (A) Compacted *Nummulites* grainstone showing abundant intraparticle megapores and some interparticle megapores. (B) *Nummulites* test showing microrhombic calcite and associated micropores. SEM image of Ar–ion-milled surface. Black specks = micropores. (C) Thin-section photomicrograph of *Nummulites* test with intraparticle pores nearly filled by calcite. (D) Same as C, but photomicrograph taken under UV light. *Nummulites* grain is microporous, as indicated by blue haze. (E) Porosity vs. permeability plot of *Nummulites* samples (modified after Loucks et al. [1998]). Area of relatively high porosities and associated low permeabilities interpreted as samples dominated by nano- and micropores.

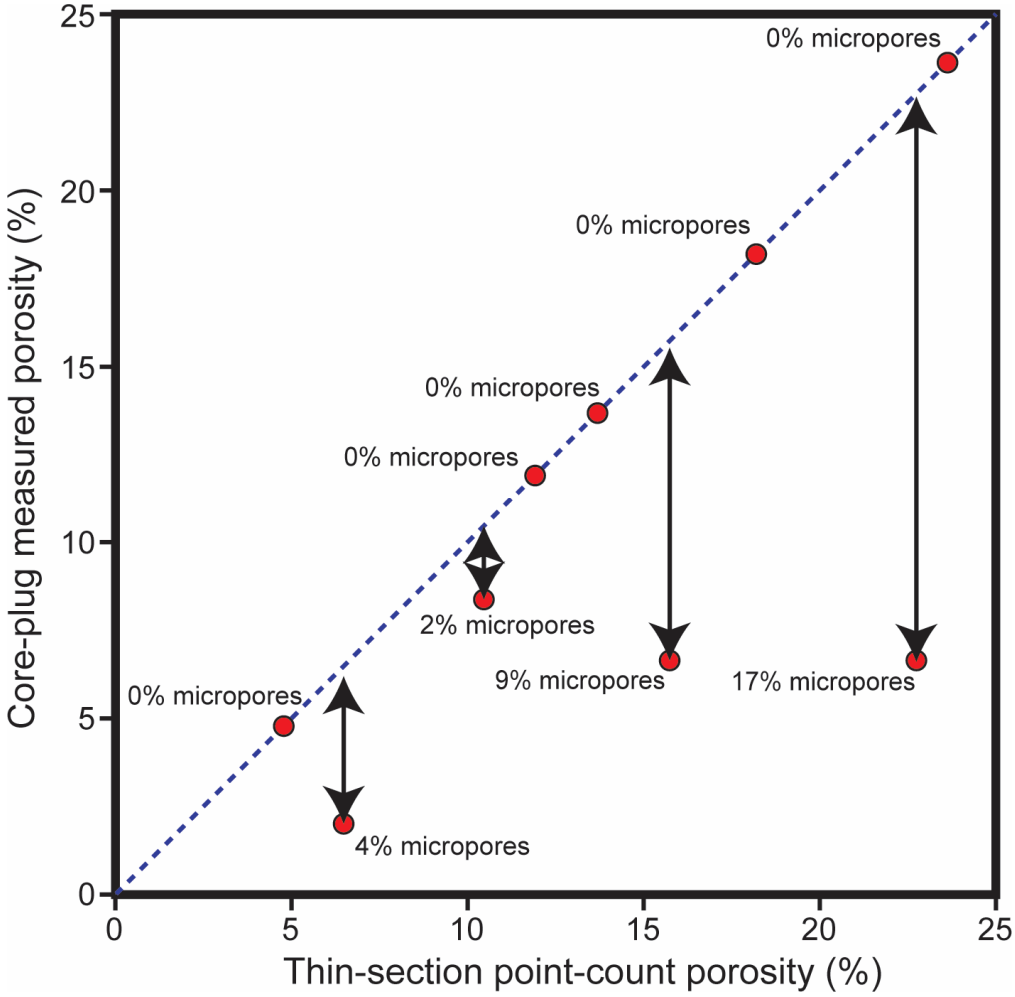

Figure 5. Diagram emphasizing method of estimating nano- and micropores by comparing thin-section point-count data with conventional core-plug analyses. If sample has no nano- or micropores, thin-section point-count porosity equals core-plug measured porosity, as shown by red dots on blue dashed line. If samples (red dots) fall below blue line, difference is attributed to nano- and micropores.

od is not possible owing to the artifacts produced when the rock is broken. Thin sections can also be viewed using SEM, especially if they are well polished, but the added epoxy in the pores may easy imaging the nano- and micropores difficult.

Pore casts (Fig. 6) are another method of imaging nano- and micropores in limestones using SEM. This method involves etching an epoxy impregnated thin-section stub with weak hydrochloric acid. A layer of calcite will dissolve and leave the epoxy-filled pores in three-dimensional relief. Pore casts are an excellent method of inaging the pore network (Fig. 6).

Nuclear Magnetic Resonance (NMR)

NMR analysis can provide porosity and pore-size distribution (e.g., Arns [2004]. Rashid et al. [2017], and Benavides et al. [2020]). Yao et al. (2010) showed that NMR transverse relaxation (T2) distributions in nano- to micropore systems strongly relate to pore size. They noted pore populations even less than 0.1 µm in size are recorded. Also, integrating NMR and MICP analysis can provide the relationship of T2–relaxation time and pore-throat size (e.g., Duan et al. [2018] and Tian et al. [2018]). Using these relationships between MICP analyses and continuous NMR analyses from wireline logs, we can obtain a continuous pore-throat-size distribution of the wireline logged section (e.g., Huang et al. [2020]). A plot of T2–relaxation time (unpublished data from a South Texas Lower Cretaceous Sligo porous ooid grainstone) displays three peaks relating to what are interpreted as nanopore, micropore, and macropore populations (Fig. 7). An associated thin-section photomicrograph of the porous ooid grainstone is shown in Figure 7A.

Mercury Injection Capillary Pressure (MICP)

MICP is probably the most common method of obtaining pore-throat-size distributions in rock samples (e.g., Schowalter [1979], Peng et al. [2017], and Tian et al. [2018]). The technique determines pore volume by calculating the volume of mercury introduced into the pore system under increasing stages of injection pressures up to 60,000 to 100,000 psi. Mercury intrudes through pore throats of a specific size at a given pressure. The Washburn equation (Washburn, 1921) is used to define the percentage of pore throats of a given radius at each specific pressure stage. A full MICP analysis over the full range of injection pressure steps provides a distribution of pore-throat radii (e.g., Figures 8E and 8F). Relative numbers of nano- and micropores are readily apparent in MICP curves and associated pore-throat-radius curves from the Upper Cretaceous Buda Chalk in South Texas (Figs. 8E and 8F). These curves (Fig. 8E) show a range of high injection pressures, 800 to 7000 psi, indicating very fine-scale pore throats. An associated distribution of pore-throats plots in the nanopore-throat range (Fig. 8F).

INTRODUCTION TO THE GENERAL SPECTRUM OF NANO- AND MICROPORE TYPES AND COMMENTS ON ORIGIN, SPATIAL DISTRIBUTION, AND CONNECTIVITY

Nano- and micropores occur in limestone and dolostone lithologies, as well as in organic matter in carbonate pores. Within each category, subcategories have their own populations of properties and their own spatial distributions. Note that combina-

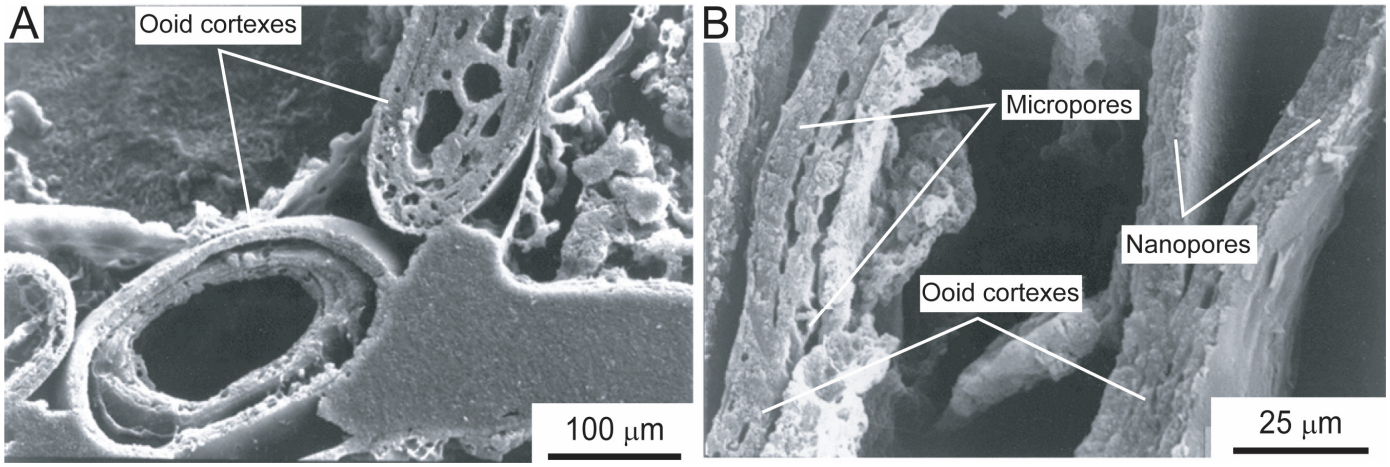

Figure 6. SEM images of thin-section-stub epoxy pore casts. (A) Pore cast of Holocene ooid grainstone from Cancun, Mexico. After etching with HCl acid, epoxy (i.e., pores) stands in relief. (B) Close-up of pore cast showing nano- and micropores. Nano- and micropores = tiny spheres.

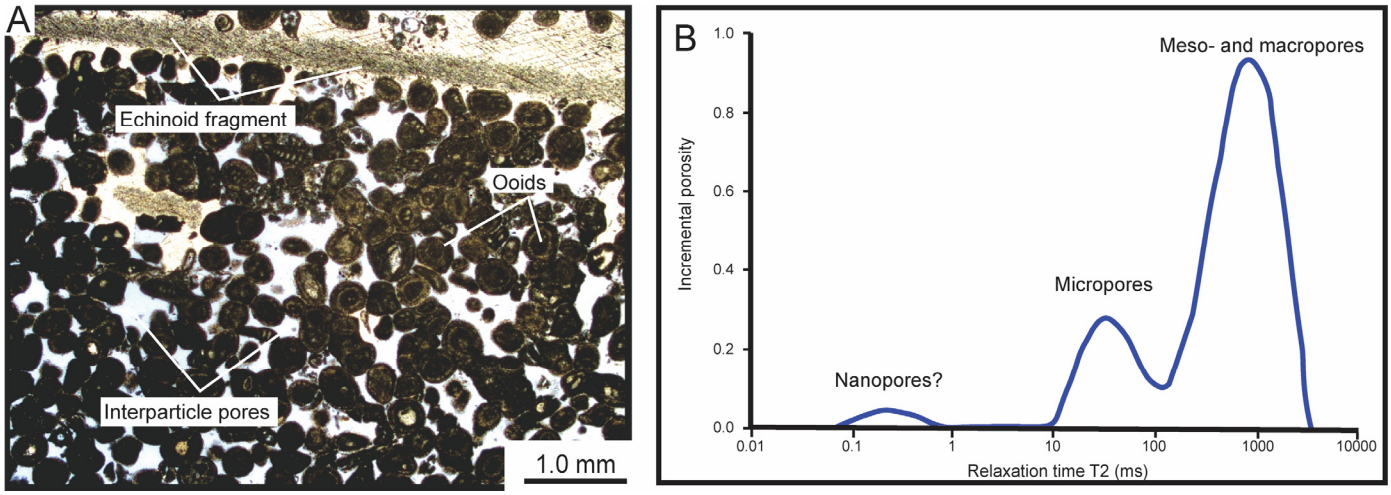

Figure 7. NMR example. (A) Lower Cretaceous Sligo ooid grainstone from South Texas containing abundant interparticle pores. Ooids contain abundant nano- and micropores. (B) NMR plot showing three populations of pore sizes.

tions of nano- and micropores of different types and origins can occur in the same rock and that the abundance of nano- and micropores in a carbonate rock can range from minor to abundant (i.e., they can dominate the entire pore network).

Nano- and micropores have many origins. Some pores are related to depositional processes, many are related to diagenetic processes, and others are produced by a combination of depositional and diagenetic processes. Diagenetic processes range from grain scale, such as stabilization of unstable mineral types, up to regional scale for diagenetic processes such as dolomitization. Handford et al. (1989) and Kaczmarek et al. (2015) reviewed some of the origins of nano- and micropores in limestones, Loucks (2017) did a preliminary review of nano- and micropores in dolostones, and Loucks et al. (2012) published a review of nano- and micropores in organic matter.

As mentioned earlier, nano- and micropores in limestones have several contrasting origins, and because of these different origins, spatial distributions of the nano- and micropores differ. Also, within each category, connectivity between nano- and micropores can vary, enabling them to form their own pore network or dual-pore networks having macropores or fractures.

In this section, each of the more common nano- and micropore types are introduced, and their origin, pore connectivity, and pore networks are discussed. Note that although this review cannot cover all occurrences of nano- and micropores, most common occurrences are discussed.

Limestones

Nano- and micropores, having several origins in limestones, can be divided into three major subcategories of rocks: (1) rocks dominated by lime mud, the original texture of carbonate sediment that is defined by grains of less the 62.5 μm; (2) chalk, which is dominated by coccolith hash; and (3) original Mg–calcite grain-rich sediment. Lime mud is deposited with abundant porosity—as much as 80% (Enos and Sawatsky, 1981)—with most pores being nano- and micropores in matrix and grains. Compaction and diagenesis both reduce initial high porosity. Chalks are composed predominately of microcrystalline coccolith elements (i.e., hash) and have abundant, very fine-scale interparticle nano- and micropores. In modern coccolith-hash muds, porosities can range up to 70% (Scholle, 1977; Fabricius and Borre,

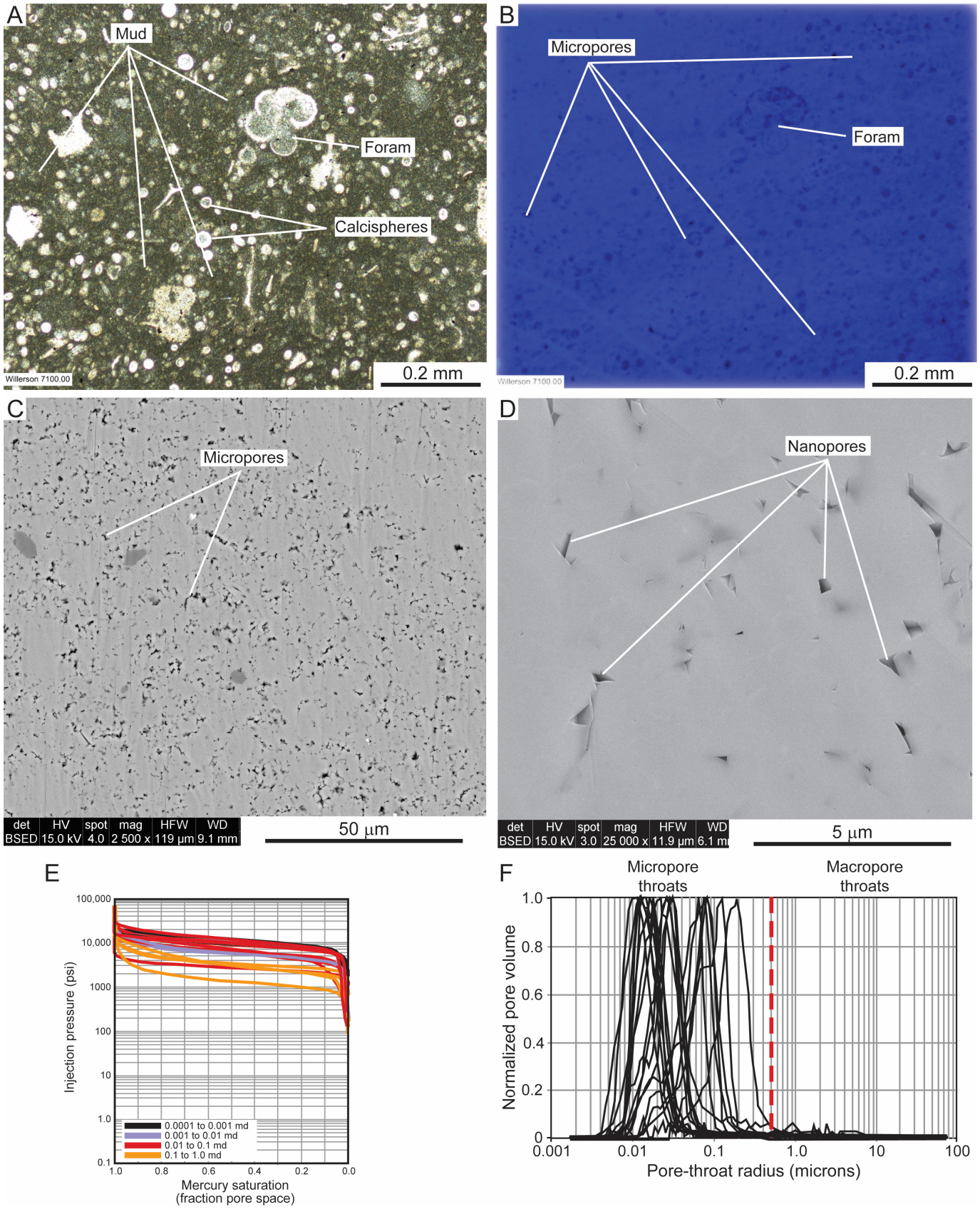

Figure 8. Microporous chalk. Upper Cretaceous Buda Formation, South Texas Comanche Platform. (A) Calcisphere planktic foraminifer lime wackestone. (B) Same as A, but photomicrograph taken under UV light. Coccolith-hash-mud matrix microporous, as indicated by blue haze. (C) SEM image of an Ar–ion-milled surface showing coccolith hash with nano- and micropores. (D) SEM image of well-cemented coccolith hash with nanopores. (E) MICP analyses showing high initial-injection-entry pressures, indicating small pore throats. Data are from Loucks et al. (2019). (F) Pore-throat distributions as calculated from MICP analyses. Most pore throats are in nano- to micropore range. Data are from Loucks et al. (2019).

2007; Fabricius et al., 2008). Mg–calcite allochems and Mg–calcite micrite envelopes transform to calcite during diagenesis (Land, 1967; Loucks et al., 2013), and nano-and micropores are inherited or develops. Each of these populations of nano- and micropores is discussed in this section.

Lime Mud

Modern lime muds are generally a mixture of very fine-grained aragonite, calcite, and Mg–calcite (Fig. 9A) (Gischler et al., 2013), and the abundance of each component varies over geologic time, depending on whether the long-term climate cycle was in a Greenhouse or Icehouse phase (e.g., Schlager [2005]). All three minerals are relatively stable in marine waters, but upon undergoing meteoric or burial diagenesis, aragonite and Mg–calcite become unstable and transform to calcite, whereas calcite remains stable (e.g., Land [1967], Loucks et al. [2013], and Lucia and Loucks [2013]). Aragonite and Mg–calcite can also form moldic pores. Some of the initial nano- and micropores between the transformed mud particles remain but decrease in abundance as compaction and cementation progress.

Aragonite mud-sized grains, common components in modern lime mud, generally occur in low-energy depositional settings in the form of aragonite needles that are 1 μm long and a few tenths of 1 μm wide (Fig. 9A) (e.g., MacIntyre and Reid [1992]). A number of studies have documented the transformation of aragonite to stable calcite (e.g., Land [1967] and Lucia and Loucks [2013]). The needles undergo dissolution and reprecipitation as microcrystals of calcite (Reid and Macintyre, 1998) (e.g., Figure 9B), and larger, Mg–calcite allochems are fragmented to mud-sized particles that accumulate in low-energy settings. As discussed later, these Mg–calcite particles transform to stable microrhombohedral calcite in a dissolution-precipitation process (Reid and Macintyre, 1998; Loucks et al., 2013). Mud-sized calcite grains form in the breakdown of larger calcite grains and these grains are generally stable during meteoric and burial diagenesis.

The origin of a nano- to micropore system in lime mud is generally the result of inherited pores (Fig. 9A), chemical stabilization of the mud particles, and compaction (Fig. 9B). Original calcite particles generally do not dissolve and can act as nuclei for calcite precipitation. Because the stabilization of aragonite and Mg–calcite produces carbonate for additional cementation, the initial unstable lime mud most likely undergoes dissolution and reprecipitation to microcrystalline calcite with associated nano- to micropores (Fig. 9B). As diagenesis progresses, compaction and cementation decrease the overall pore space. During advanced diagenesis, nearly all pores may disappear, as is common in many lime mudstones and wackestones (e.g., Steinen [1978]).

Distribution of nano- and micropores in stabilized lime mud varies and depends on the level of energy in the depositional setting and resulting depositional textures. Because mudstones, wackestones, and packstones all contain lime mud, vertical and lateral distribution of these carbonate textures, which contain nano- and micropores, will control the distribution of lime mud-related nano- and micropores. A lithofacies analysis of their spatial distribution, integrated with a pore-type description, is the basis for discerning nano- and micropore spatial distribution.

Connectivity of nano- and micropores in mud-dominated limestones reflects original connectivity in the unlithified mud. Pores may not be common, and pore throats will be very fine, resulting in low permeability. Loucks (2002) showed quantitatively that the amount of mud in a limestone is inversely related to porosity and permeability.

Chalk

Chalks are composed primarily of fragments of coccolithophores (unicellular phytoplanktonic algae) (Figs. 8 and 10–12), and constituents include coccoliths and disaggregated coccolith elements (e.g., Figures 12B and 12C). Other organisms such as planktic foraminifers and calcispheres are also common (e.g.,

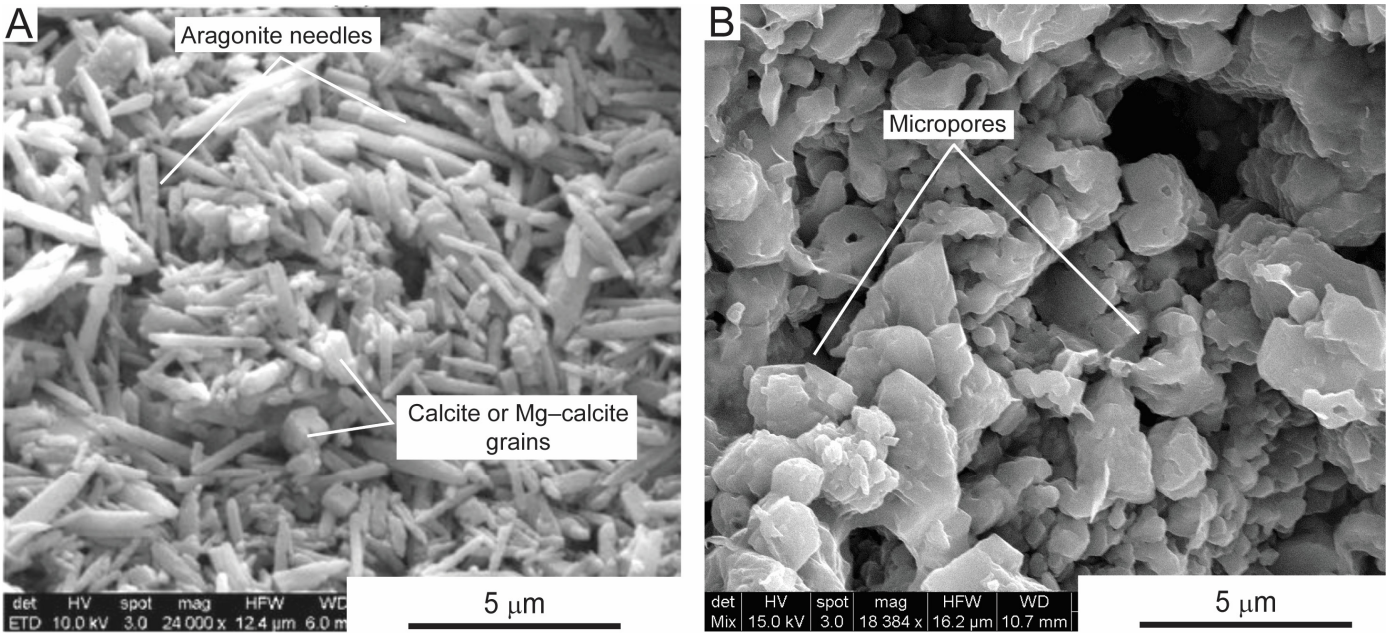

Figure 9. Example of modern and ancient carbonate muds. (A) SEM image of modern carbonate mud from Bahamas. Mud is dominated by aragonite needles, but some calcite or Mg–calcite grains are present. Note initial high number of micropores. (B) SEM image of carbonate mud from Miocene of offshore Indonesia. Poor sorting and irregular shapes of microcrystals are interpreted to result from stabilization of mixed mineralogy and shallow burial depth of 2931 ft (893.4 m), which precluded extensive burial diagenesis.

Figure 12A), but coccolith hash controls the overall pore network.

Coccolithophores are calcite in composition and, therefore, are relatively stable during early burial diagenesis (Scholle, 1977). Although at shallow burial depths, chalks have high porosities (up to 70%) (Fabricius and Borre, 2007; Fabricius et al., 2008), with burial they lose pore space through compaction. At depths of ~300 ft (~100 m), porosity can be reduced to below 25%. At burial depths in the range of 2460 ft (750 m), some dissolution of coccolith hash initiates (Fabricius and Borre, 2007), and dissolved carbonate precipitates around the coccolith elements, producing microrhombs of calcite with associated nano- and micropores between them (e.g., Figures 10B and 12D) (Scholle, 1977; Loucks et al., 2021). The resulting pore network is composed of interparticle nano- and micropores (Figs. 8 and 10–12).

Nano- to micropores in chalks are generally well connected because the pores occur between coccolith-hash elements that dominant the system; however, minor detrital or authigenic clay flakes can occur in the interparticle pores, reducing pore-throat diameters and, hence, permeability (Loucks et al., 2021). Although the regional distribution of chalk deposition will be the first level of control on the spatial distribution of these pore types, within chalk, different chalk lithofacies can have an effect on the number of nano- and micropores. Loucks et al. (2021) showed that for the Austin Chalk along the onshore northern Gulf of Mexico, the number of nano- and micropores varies by lithofacies. See table showing porosity and permeability statistics for the Austin Chalk (Fig. 10E). See Loucks et al. (2021) for details about different Austin Chalk lithofacies (Fig. 7).

Statistical analysis (47 modified gas-expansion analyses obtained by the method of Peng and Loucks [2016] and Peng et al. [2017]) in Loucks et al. (2021) shows that porosity was highest in slightly argillaceous, burrowed marly chalks (5.5–6.2%) and lowest in organic-rich, laminated marly chalks and chalky marls (3.5–4.5%).

Mg–Calcite and Micrite

Mg–calcite-rich allochems (e.g., larger foraminifers, red algae, bryozoans, stromatoporoids, *Lithocodium*, and Mg–calcite ooids) and Mg–calcite micrite envelopes are chemically unstable and transform to microrhombic calcite and associated nano- and micropores as they stabilize (Loucks et al., 2013) (Figs. 13–15). In this subcategory, Mg–calcite nano- and micropores are controlled by the abundance and distribution of original Mg–calcite grains.

Many Mg–calcite allochems were originally composed of Mg–calcite rods a few microns long with nanopores between the rods (Reid and Macintyre, 1998; Loucks et al., 2013). Reid and Macintyre (1998) and Loucks et al. (2013) demonstrated that these microrods break down into nanospheres (i.e., spheres in the nanometer range) by dissolution and precipitate overgrowths to form microcrystalline calcite with associated nano- to micropores (e.g., Figure 15C). The resulting pore network is constrained to the grain and/or matrix and generally forms variable spatial distributions of nano- and micropores (Fig. 2G).

Micrite envelopes form by microalgae and fungi boring into carbonate allochems and producing a rim around the allochems (Windland, 1968) (e.g., Figure 15A). These Mg–calcite envelopes stabilize to microrhombic calcite with associated micropores (e.g., Figure 2G). Commonly, if the precursor mineralogy of an was aragonite, only the micrite envelope would be preserved, and the original aragonite portion of the allochem would be a moldic pore or cement-filled pore.

Diagenetic transformation of Mg–calcite is allochem specific. The distribution of nano- and micropores will be controlled by the original distribution of Mg–calcite allochems and micrite envelopes. Original distribution of Mg–calcite allochems can be established by thin section on the basis of petrographic analysis to define lithofacies and their distribution. Note that not all Mg–calcite grains always transform to nano- and micropores (e.g., echinoderms), and even some grains that commonly transform to nano- and micropores may not develop nano- and micropores under some diagenetic conditions. Loucks et al. (2013) also showed that following development of nano- and micropores, later cementation can occlude these pores.

A ternary diagram of the occurrences of nano- to micropores in former Mg–calcite-rich carbonate rock shows three end members: (1) former Mg–calcite grains, (2) micrite envelopes, and (3) former Mg–calcite-rich matrix (lime mud) (Fig. 16). In Mg–calcite-rich carbonate rocks, connectivity will depend not only on the number of nano- to micropores, but also on the spatial distribution of former Mg–calcite microporous elements (e.g., Figures 2G, 13A, 14B, 14D, 15B, and 16). The transformed Mg–calcite grains have nano- to micropores internally within their grain boundaries, forming an isolated domain of pores (Fig. 2G). Unless the grains are in contact with other porous grains or porous matrix, the nano- to micropores may be isolated and most likely do not contribute to the effective pore system. The micrite envelopes contain nano- to micropores in a rim surrounding the host grain (e.g., Figure 2G). Again, unless these rims are in contact with other porous grains or matrix, they will be isolated rims of pores. Therefore, for both former Mg–calcite grains and micrite envelopes, an effective pore system requires the grains to be touching each other or to be connected to each other by a microporous matrix (e.g., Figures 13C–13F). In a grainstone, former Mg–calcite grains and micrite envelopes may be isolated by nonporous-cement pore fill because grain-to-grain contact may be limited (e.g., Figures 13A and 13B). Former Mg–calcite-dominated mud matrix (e.g., wackestones and packstones) can supply a connecting medium of nano- to micropores that allows a continuous pore network. Other pore types, such as interparticle pores, will also help to provide connectivity to various nano- to micropores.

Dolostones

Three major subcategories are also defined in dolostones, in which one subcategory results from extensive whole-rock replacement (overdolomitization), a second subcategory related to differential dolomite precipitation and replacement results in dolomitization at the allochem and matrix scale, and a third subcategory is related to inherited pores from the precursor microporous limestone. Concepts of nano- and micropore development in dolostones are more speculative than in limestone because dolomitization is a complex process and commonly masks several earlier stages of diagenesis. Development of nano- and micropores in dolomites is generally related to diagenesis, except where nano- and micropores are inherited from the precursor limestone. Dolomitization is a multifaceted diagenetic process (e.g., Machel [2004]), and alteration of the precursor limestone can produce variable textures and fabrics, as well as associated pore types and networks. Both megapores (e.g., intercrystalline [i.e., interparticle] and moldic) and nano- and micropores result from the dolomitization process.

Discussion of the distribution of nano- and micropores in dolomites is difficult because the origin of the dolomitization process is generally questionable and several dolomitization stages are common (e.g., Machel [2004]). Therefore, a precise outline of an approach to identifying nano- and micropore spatial distribution in many dolostones may be impossible.

Inherited Nano- and Micropores from Precursor Limestone

Dolomitization of a nano- to microporous limestone may preserve some of the original nano- and micropores (inherited pores; e.g., Figures 17 and 18). In order to explain

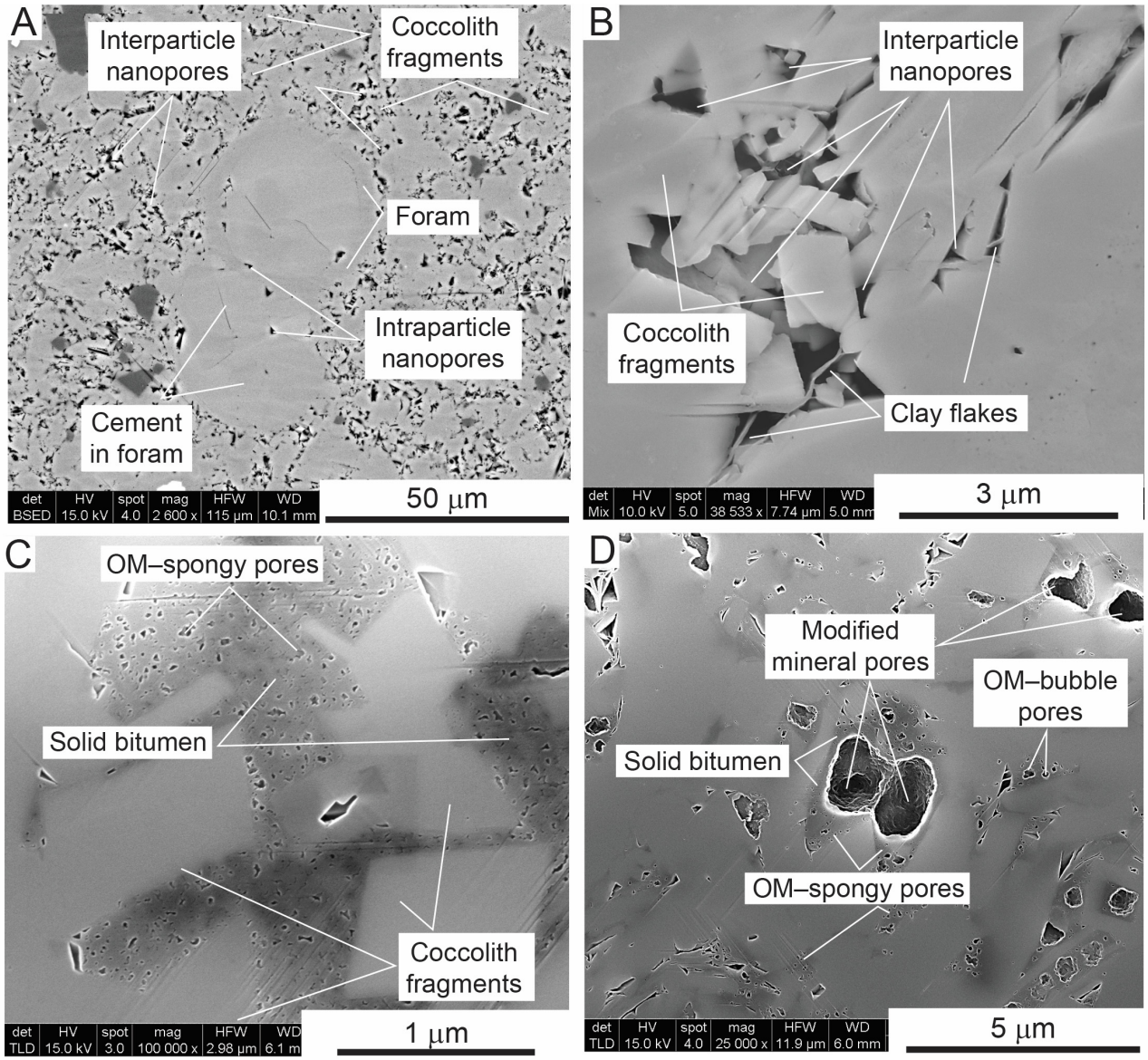

E

	Mean	Std. dev.	Count	Minimum	Maximum	Geom. mean
Porosity of all analyses (%)	5.0	2.1	47	0.5	8.5	
Burrowed marly chalk (lithofacies 1) porosity (%)	6.2	1.6	13	3.5	8.5	
Burrowed chalky marl (lithofacies 2) porosity (%)	5.5	1.3	14	3.8	7.6	
Laminated marly chalk (lithofacies 3) porosity (%)	4.5	2.9	7	0.5	8.0	
Laminated chalky marl (lithofacies 4) porosity (%)	3.5	1.8	13	0.9	6.1	
Permeability of all analyses (nd)	402	673	47	3	3375	121
Burrowed marly chalk (lithofacies 1) permeability (nd)	704	894	13	28	3375	351
Burrowed chalky marl (lithofacies 2) permeability (nd)	445	612	14	39	2006	214
Laminated marly chalk (lithofacies 3) permeability (nd)	432	752	7	3	2111	101
Laminated chalky marl (lithofacies 4) permeability (nd)	38	29	13	4	88	25

Figure 10. Microporous chalk. Upper Cretaceous (upper Turonian to lower Campanian) Austin Formation, onshore northern Gulf of Mexico. (A) Microporous chalk with cement-filled planktic foraminifer. Dark spots = nanopores. SEM image of Ar–ion-milled surface. (B) Close-up of chalk with interparticle nanopores, some bisected with authigenic clay plates. SEM image of Ar–ion-milled surface. (C) Interparticle nanopores between coccolith fragments filled with solid bitumen containing spongy pores. SEM image of Ar–ion-milled surface. (D) Sample showing modified mineral pores, bubble pores, and spongy pores. SEM image of Ar–ion-milled surface. (E) Statistics showing porosity and permeability of four general lithofacies within Austin Chalk, as defined by Loucks et al. (2020). Table from Loucks and Peng (2021).

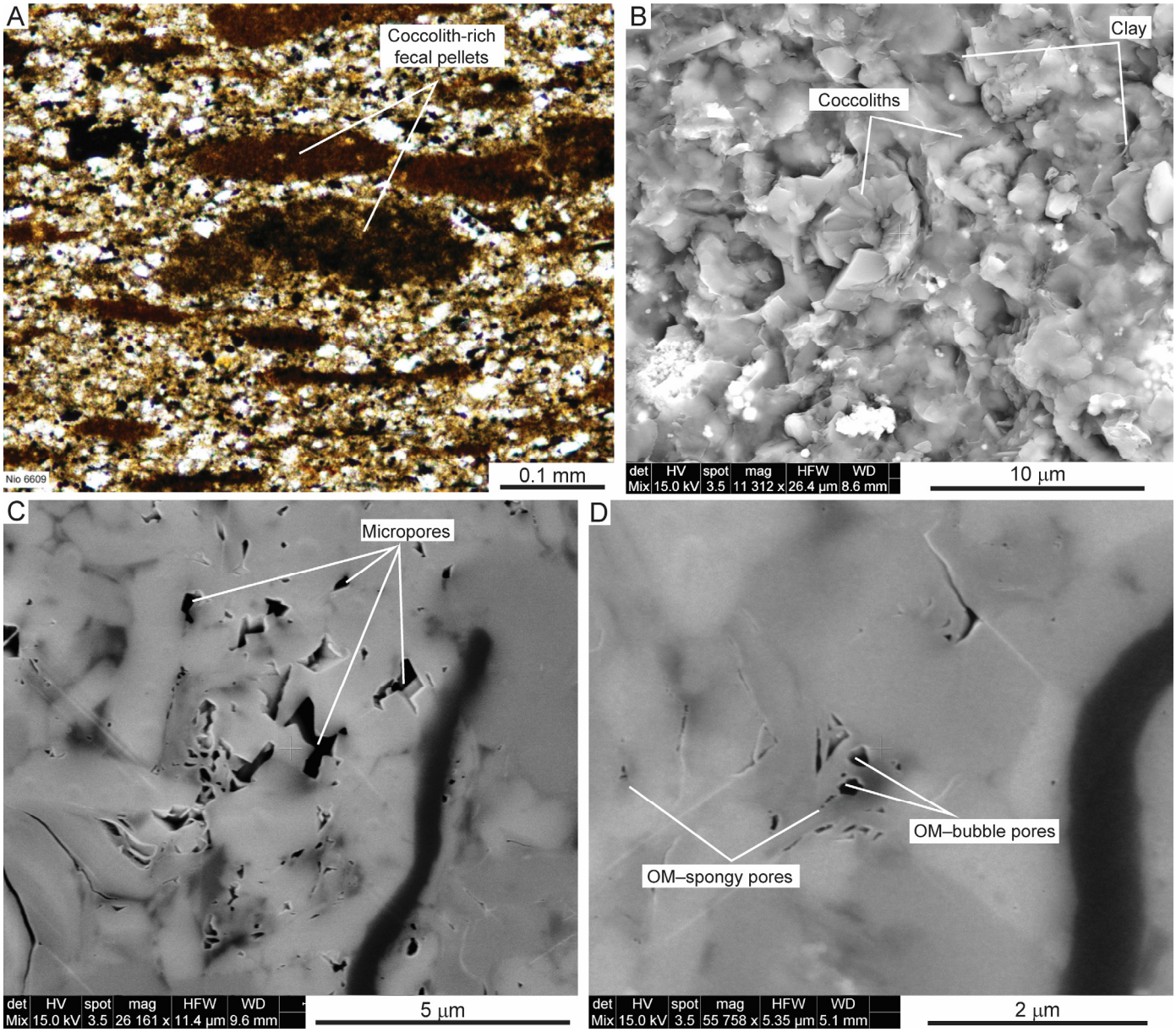

Figure 11. Microporous chalk. Upper Cretaceous (upper Turonian to lower Campanian) Niobrara Formation in northwestern Colorado area of Western Interior Seaway. (A) Thin-section photomicrograph of argillaceous pelletal chalk. These pellets are most likely fecal product of copepods and are composed of coccolith fragments. Anoxic environment allowed pellets to be preserved (Loucks and Rowe, 2014). (B) SEM image of rock chip showing well-cemented coccolith hash with nanopores, micropores, and clays. (C) Coccolith hash with interparticle nanopores, micropores, and some organic-matter pores. SEM image of Ar–ion-milled surface. (D) Close-up of organic-matter pores in solid bitumen. SEM image of Ar–ion-milled surface.

the distribution of inherited nano- and micropores from a precursor limestone, an understanding of the original pore-system distribution in the limestone is required, which is difficult because the dolomitization process commonly obscures the texture and fabric of the original limestone. Even though challenging, however, an attempt should be made to identify distribution of the original limestone lithofacies and the relationship of nano- and micropores to the original limestone lithofacies. And then an assessment of what initial pores survived the dolomitization process should be made. A relationship between inherited nano- and micropores and initial limestone lithofacies distribution may exist.

Pore connectivity related to inherited nano- to micropores in dolostones depends on an original connectivity within the limestone precursor. Also, the dolomitization process itself can develop new pores that can enhance connectivity of inherited nano- to micropores.

Whole-Rock Overdolomitization

Before a limestone is dolomitized, it may initially have abundant pores, but the dolomitization process may be extensive enough to not only dolomitize the framework, but also nearly occludes the associated pore network. This extensive dolomitization results from an open-flow system where addition dolomitizing fluids are available. Lucia (2004) and Machel (2004) labeled this dolomitization process overdolomitization. The remaining pore network consists of nano- and micropores (Fig. 19).

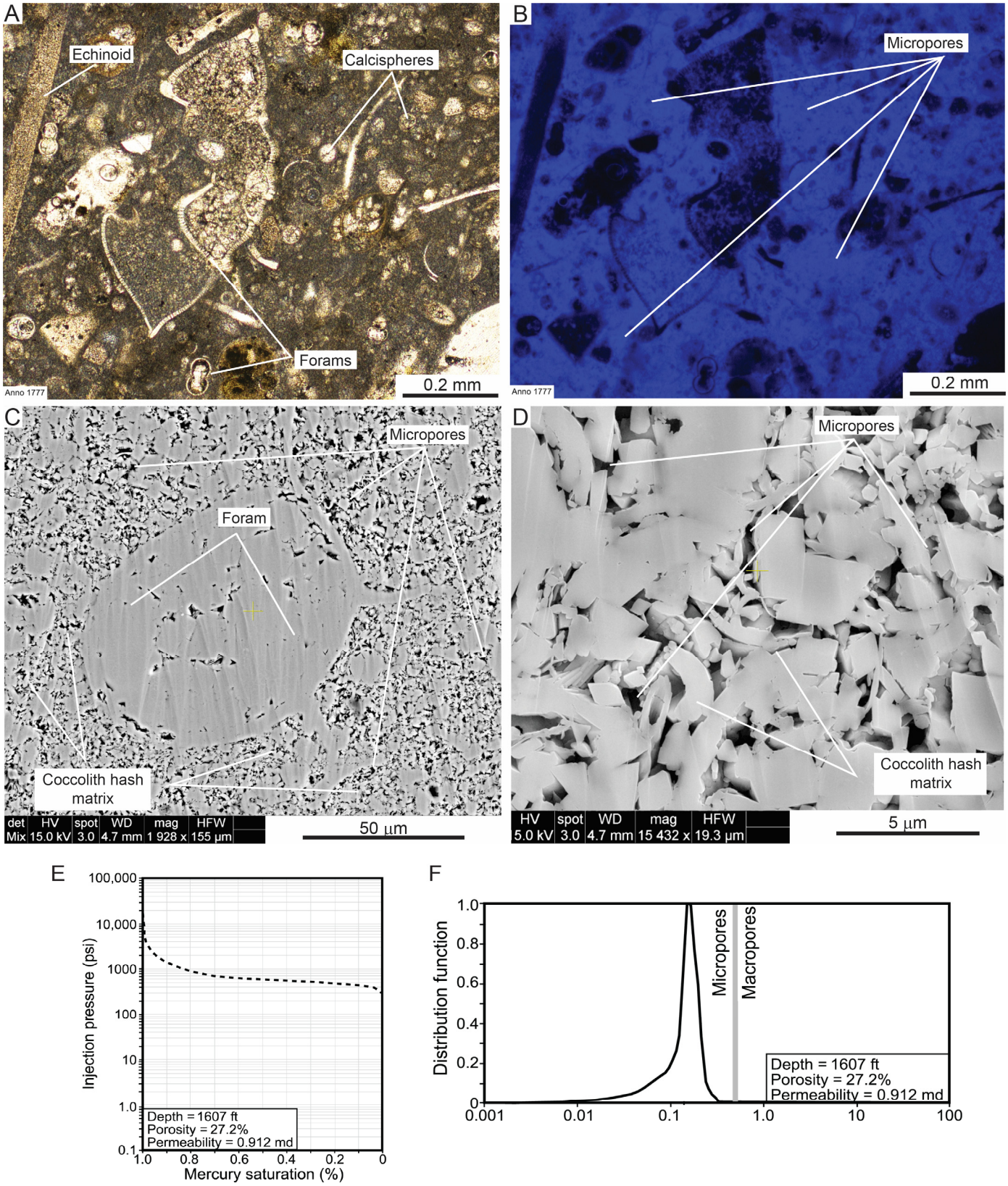

Figure 12. Microporous chalk. Upper Cretaceous (Campanian) Annona Chalk, drowned Comanche Platform in northwestern Louisiana. (A) Coccolith planktic-foraminifer lime packstone. Matrix is coccolith hash. (B) Same as A, but photomicrograph taken under UV light. Coccolith-hash-mud matrix is microporous, as indicated by blue haze. (C) Matrix of chalk composed of coccolith hash with abundant micropores. Larger planktic foraminifer are present. SEM image of Ar–ion-milled surface. (D) Close-up of coccolith hash with micropores (from Loucks et al. [2017]). SEM image of Ar–ion-milled surface. (E) MICP analysis of Annona Chalk sample showing high initial injection pressure. (F) Plot of pore-throat-size distribution from MICP analysis (from Loucks et al. [2017]). Pore throats are all in micropore-throat range.

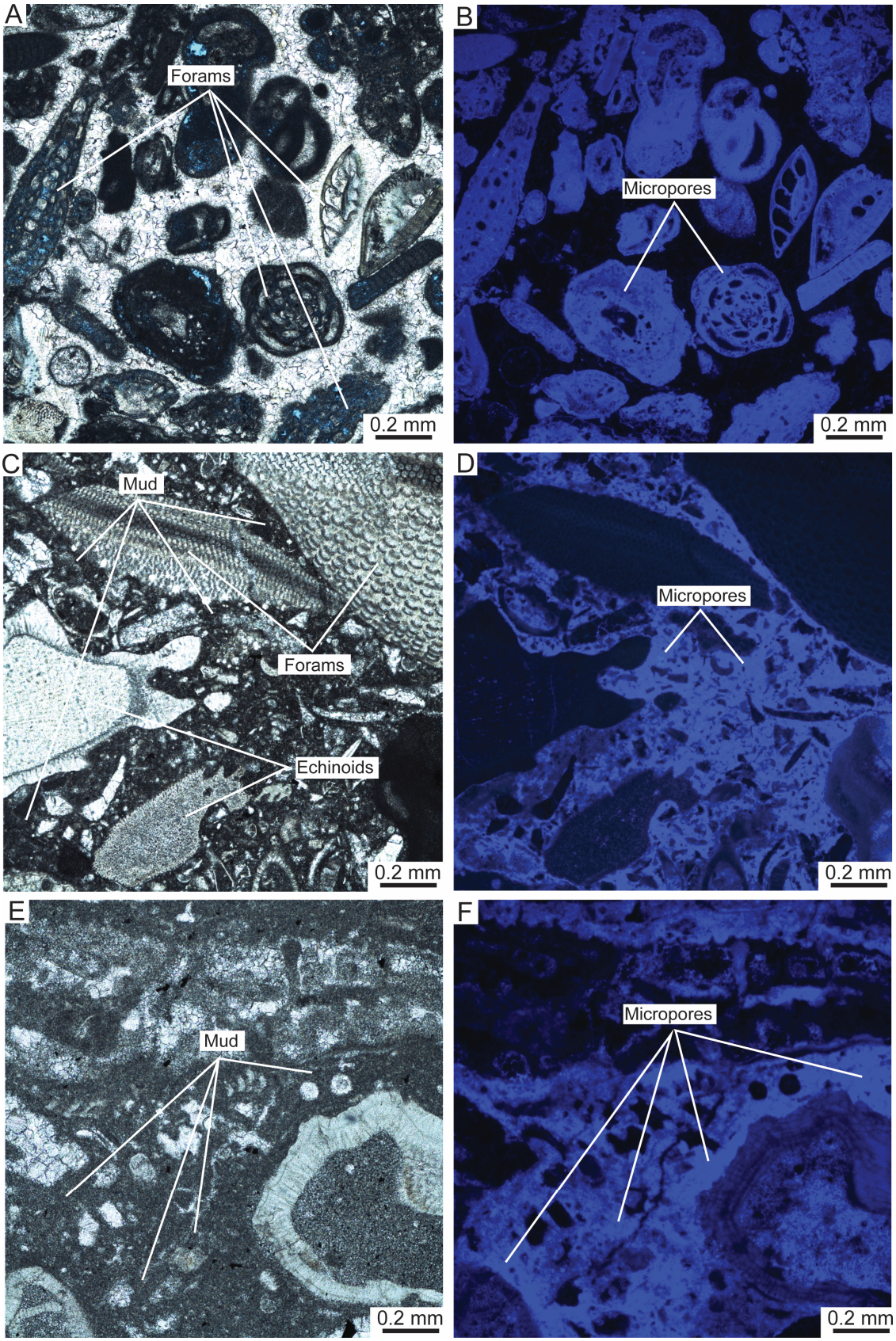

Figure 13. Microporous lime-mud matrix. Lower Miocene Nido Formation reef complex, offshore Palawan area, Philippines. (A) Well-cemented foraminifer grainstone. (B) Same as A, but photomicrograph taken under UV light. Former Mg–calcite allochems are now microporous, as indicated by blue haze. (C) Echinoid fragment and foraminifer packstone. (D) Same as C, but photomicrograph taken under UV light. Mud matrix shows blue haze, indicating microporous matrix. (E) Lime skeletal wackestone. (F) Same as E, but photomicrograph taken under UV light. Mud matrix showing blue haze, indicating microporous matrix.

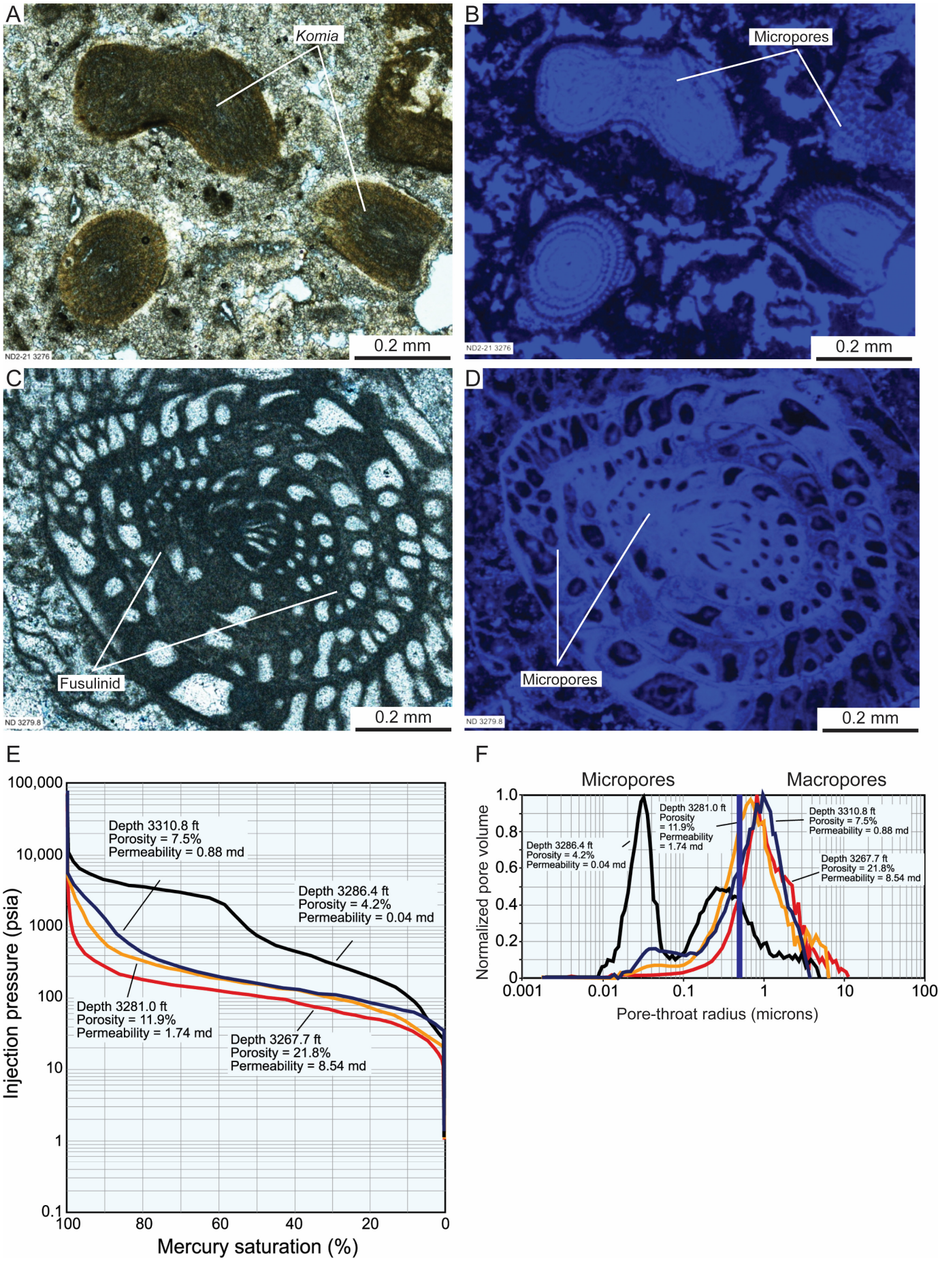
A
Komia
0.2 mm
ND2-21 3276
B
Micropores
0.2 mm
ND2-21 3276
C
Fusulinid
0.2 mm
ND 3279.8
D
Micropores
0.2 mm
ND 3279.8
E
Depth 3310.8 ft
Porosity = 7.5%
Permeability = 0.88 md
Depth 3286.4 ft
Porosity = 4.2%
Permeability = 0.04 md
Depth 3281.0 ft
Porosity = 11.9%
Permeability = 1.74 md
Depth 3267.7 ft
Porosity = 21.8%
Permeability = 8.54 md
Injection pressure (psia)
100,000
10,000
1000
100
10
1
0.1
100
80
60
40
20
0
Mercury saturation (%)
F
Micropores
Macropores
Depth 3281.0 ft
Porosity
= 11.9%
Permeability
= 1.74 md
Depth 3310.8 ft
Porosity = 7.5%
Permeability = 0.88 md
Depth 3286.4 ft
Porosity = 4.2%
Permeability = 0.04 md
Depth 3267.7 ft
Porosity = 21.8%
Permeability = 8.54 md
Normalized pore volume
1.0
0.8
0.6
0.4
0.2
0
0.001
0.01
0.1
1
10
100
Pore-throat radius (microns)

(FACING PAGE) Figure 14. Mg–calcite-dominated microporous rocks. Pennsylvanian (lower Desmoinesian) Caddo Formation in north-central Texas. (A) *Komia* lime packstone. *Komia* mineralogy originally Mg–calcite. (B) Same as A, but photomicrograph taken under UV light. *Komia* grains are microporous, as indicated by blue haze. (C) Fusulinid grain where intraparticle pores are filled with calcite cement. (D) Same as C, but photomicrograph taken under UV light. Fusulinid grain is microporous, as indicated by blue haze. (E) MICP analysis of several Caddo samples showing moderate initial injection pressures. Slope of injection curves shows wide range of pore-throat sizes (from Loucks and Fu [2016]). (F) Plot of pore-throat-size distribution from MICP analysis (from Loucks and Fu [2016]). Pore throats show range of values with many in micropore range.

By definition, overdolomitization partly or completely obscures limestone textures and fabrics. If the texture and fabric are unrecognizable, then the original lithofacies distribution might not be discernable enough to help define distribution of the nano- and micropores. In this case, an attempt can be made to map out areas that are overdolomitized and assume that nano- and micropores may be present in these areas; however, their abundance may be minor.

Pore connectivity in dolostones that show overdolomitization will depend on the degree of dolomitization. If the process ends before all pore throats are cemented, some connectivity will be preserved, and resulting permeability will depend on sizes of the remaining pore throats (e.g., Bliefnick and Mariotti [1988]), although with the nanopores occurring at crystal boundaries, permeability will be low. At the meter scale, connectivity in an overdolomitized rock would probably be homogeneous.

Differential Dolomitization at Allochem and Matrix Scale

Differential dolomite cementation and allochem replacement is related to the fabric of the precursor limestone. Allochems or matrix may be more intensely dolomitized, resulting in small-scale dolomitization differences and strong heterogeneity in pore-size distribution in the rock. Some areas may be nearly completely cemented; however, in other areas, common nano- to micropores are preserved. Some megapores may also be preserved (Fig. 20), and the dolomitization process can create many variations on this theme.

As mentioned earlier, dolomitization is a multifaceted process and the resulting dolostone texture and fabric can vary depending on the original limestone texture and fabric, as well as the dolomitization process (e.g., Machel [2004]). A detailed discussion of dolomitization processes (i.e., models) is beyond the scope of this nano- and micropore review (see Machel [2004] for an in-depth review).

In porous limestones (e.g., grainstones), differential dolomitization can produce variations in the final dolostone texture, fabric, and resulting pore-size differences (Fig. 20). In interparticle-pore areas, larger crystals (fine crystalline and larger) of dolomite may precipitate and fill some or all of the pores (e.g., Figure 20A). Allochems may be replaced by micron-sized dolomite crystals, and nano- and micropores are preserved (Figs. 20C and 20D).

Again, the complexities and fabric-obscuring processes of dolomitization make explaining the spatial distribution of nano- and micropores difficult. An understanding of why differential dolomitization exists within different limestone lithofacies will help in defining which dolomitized lithofacies will contain nano- and micropores. For differential dolomitization, a detailed diagenetic investigation is necessary to explain resulting dolomite patterns that will help define the distribution of nano- to macropores.

Much of the resulting differential dolomitization and associated connectivity depends on complexities of the original limestone texture, fabric, and pore types and their distribution. Connectivity from this finer-scale differential dolomitization process is therefore difficult to define at the large scale.

Fluid Inclusions in Dolomite Crystals

Fluid inclusions, common in dolomite crystals—especially in larger crystals such as saddle dolomite (Radke and Mathis, 1980)—are actually disconnected nanopores. As can be seen in saddle dolomites of the Lower Ordovician Ellenburger Group in Central Texas (Fig. 21), fluid inclusions can be abundant (approximately 20–30% in samples shown in Figure 21). These fluid inclusions can contain brines and hydrocarbons that may affect wireline-resistivity curves, as well as porosity (i.e., density) curves. However, these pores are not connected and will not add to the effective pore system. Identification of these nanopores may be crucial to an understanding of petrophysical measurements. Distribution of this dolomite nanopore type can be estimated by identifying fluid-inclusion-rich dolomites and relating the dolomites to lithofacies.

Organic Matter in Carbonates

Some carbonates, such as the Upper Cretaceous Eagle Ford Group and Austin Chalk Formation along the Texas Gulf Coast, are deposited with abundant organic matter (e.g., Reed and Ruppel [2012], Alnahwi and Loucks [2019], and Loucks et al. [2021]). Although organic matter can be original kerogen, it is more commonly thermally generated solid bitumen. Both types of organic matter can have nano- and micropores (Figs. 22 and 23) (Loucks et al., 2009; Ko et al., 2017b). Loucks et al. (2009) identified nano- to micropores in solid bitumen in the siliciclastic Barnett Shale, establishing that these fine pores can be an effective pore network in tight, unconventional reservoirs. Later studies (e.g., Loucks and Rowe [2014]; Pommer and Milliken [2015], Ko et al. [2017b], Loucks and Peng [2021], and Loucks et al. [2021]) have shown that these nano- to micropores in solid bitumen are parts of the effective pore systems in the Eagle Ford (Fig. 24), Austin (Fig. 10), and Niobrara (Fig. 11) argillaceous chalks. Although solid bitumen nano- to micropores are the most common pore type in organic matter, nano- and micropores are much less common in kerogen.

Kerogen

Type III woody kerogen commonly contains original organic-matter pores (Reed, 2017); however, these pores do not generally survive burial and thermal maturation (Fig. 22) (e.g., Loucks et al. [2012] and Loucks and Reed [2014]). These types of nano- and micropores are relatively rare because the percentage of woody material is low in most carbonates. Other kerogen types, such as type I and II algal kerogen, may have some initial pores (Figs. 23A and 23B) and commonly develop nano- to micropores during thermal maturation (e.g., Loucks et al. [2012] and Ko et al. [2016, 2017a, 2017b]).

Solid Bitumen

Most organic-matter nano- to micropores associated with carbonates form in migrated bitumen after thermal maturation (Fig. 23C–23D) (e.g., Loucks et al. [2012]). In carbonates, such as the argillaceous Eagle Ford Group and Austin Chalk, these

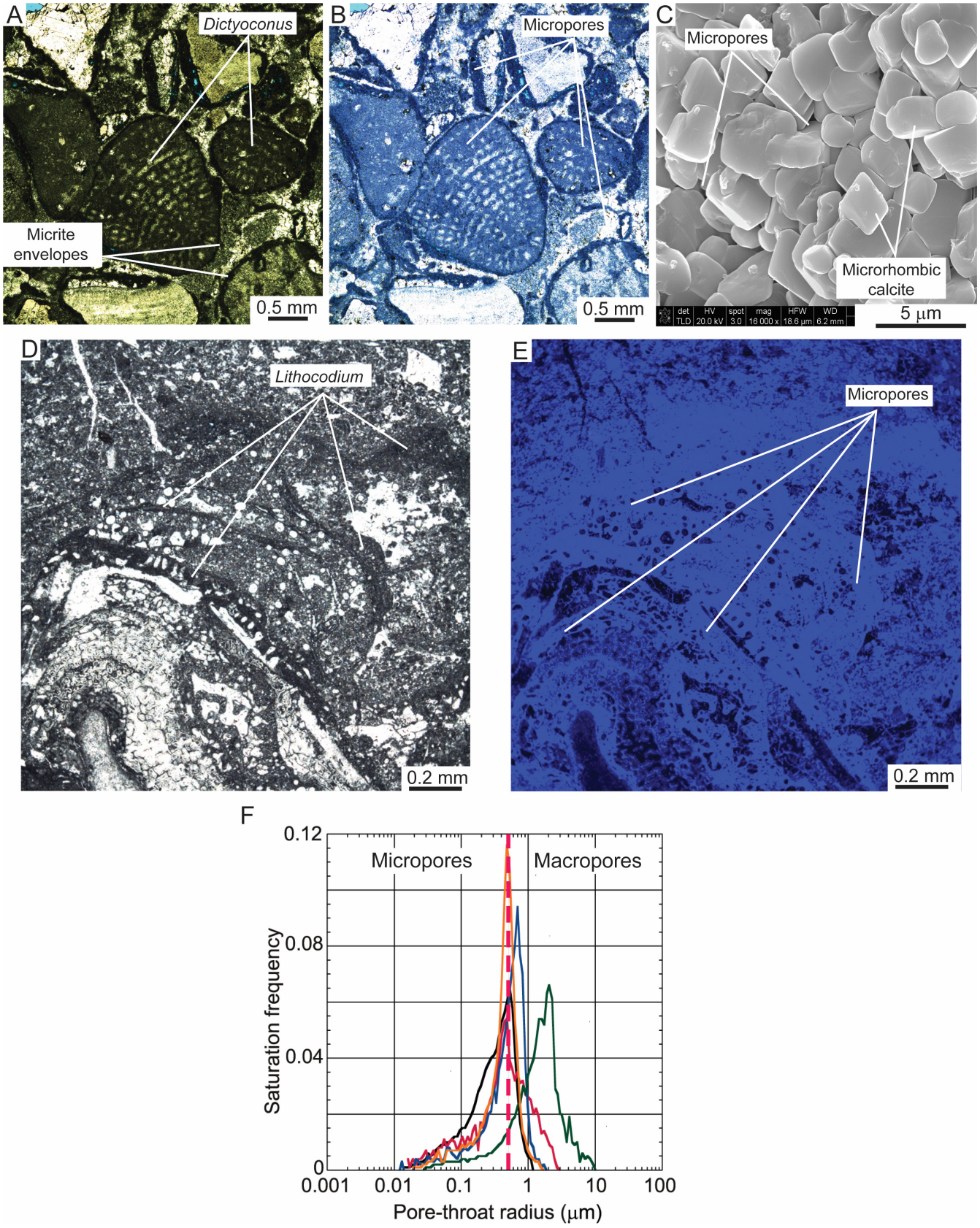

Figure 15. Mg–calcite-dominated microporous rocks. Lower Cretaceous (Albian) Stuart City Reef Trend (Edwards), South Texas Comanche Platform. (A) *Dictyoconus* packstone with micrite envelopes rimming grains. (B) Same as A, but photomicrograph taken under UV light. *Dictyoconus* grains and micrite envelopes are microporous, as indicated by blue haze. (C) Microrhombic calcite and associated micropores in *Dictyoconus* grain. SEM image of rock chip. (D) *Lithocodium* packstone. (E) Same as D, but photomicrograph taken under UV light. *Lithocodium* clusters are microporous, as indicated by blue haze. (F) Plot of pore-throat-size distribution from MICP analysis (from Loucks et al. [2013]). Pore throats showing range of values, with many in micropore range.

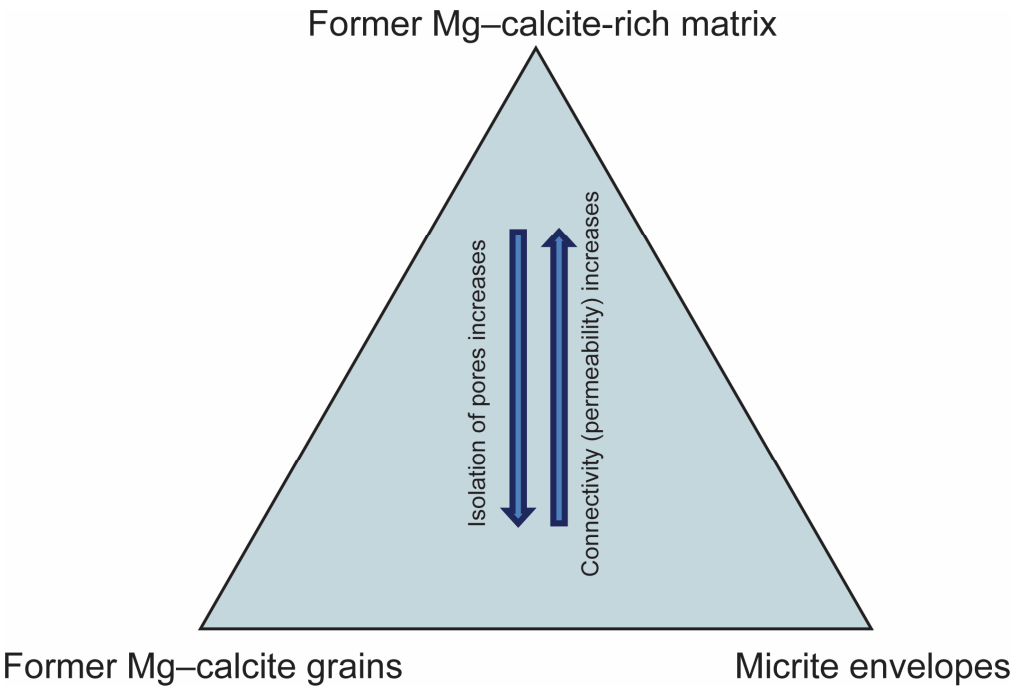

Figure 16. Ternary diagram of occurrences of nano- and micropores. Nano- and micropores can occur in three general areas, as indicated by ternary plot. Grains, micrite envelopes, and matrix represent end members.

bitumen-based nano- and micropores can contribute to the effective pore network (Figs. 10 and 24) (e.g., Pommer and Milliken [2015], Ko et al. [2017b], and Loucks and Peng [2021]).

As kerogen undergoes thermal maturation, oil and liquid bitumen are expelled from the kerogen and migrate into adjacent pores (e.g., Loucks et al. [2009] and Loucks and Reed [2014]). With further thermal maturation, some liquid bitumen transforms into solid bitumen, and within this solid bitumen, nano- to micropores form (e.g., Loucks and Reed [2014], Loucks et al. [2009, 2012], Ko et al. [2017b], and Reed et al. [2020]). Organic-matter nano- to micropores are common pore types in some unconventional, tight carbonates such as the Eagle Ford Group (Fig. 24), Austin Chalk (Fig. 10), and Niobrara Formation (Fig. 11) (e.g., Loucks and Reed [2014; Loucks and Rowe [2014], Ko et al.[2017b], Loucks et al.[2020], and Loucks and Peng [2021]) and form a significant part of the effective pore system. Because these pores are related to thermal maturation, they do not develop until vitrinite reflectance (R_o) levels of 0.6 to 0.7% are reached (Loucks et al., 2009). In some mineral micropores that contain migrated solid bitumen, not all the water has been displaced, and bubble-filled nanopores remain (Ko et al., 2016, 2017b). Although this type of organic-matter pore is unrelated to thermal maturation of bitumen, it is a fluid-displacement process.

In conventional reservoirs having a megapore system, migrated liquid bitumen and oil may transform to solid bitumen. During enhanced thermal maturation, the solid bitumen may develop nanopores, as noted in the previous discussion of chalks or as in some megapore systems seen in the Clear Fork Formation (Fig. 23); however, if pores with solid bitumen are not well connected to the effective pore system, they will not impact reservoir connectivity.

In tight carbonates impregnated with nano- to micropore-bearing solid bitumen, a continuous network of solid bitumen is necessary to produce an effective pore network. Permeability is low (in nanodarcy range) because the dominant pore type is nanopores. Overall, connectivity is effective, but because of the dominance of nanopores, hydraulic fracturing is necessary to produce these reservoirs.

Pulverulite

Pulverulite is a form of microporous limestones and dolostones in which the nano- to micropore system has been greatly enhanced by weathering at an unconformity (Fig. 25) (Kahle, 2012; Loucks et al., 2018). Loucks et al. (2018) documented the stages of enhancement of nano- to microporous pulverulitic mudstones, wackestone, and packstones in Lower Cretaceous strata in Central Texas. In outcrop, the final weathering product is a loose, micron-sized powder (Fig. 25). Microrhombohedral crystals show distinct evidence of pitting created by dissolution (Fig. 25D). This enhancement of a microporous reservoir-grade rock is restricted to within tens of meters below the surface (Deville de Periere et al., 2011), and, as noted later, pulverulite formation at unconformities can, in turn, form hydrocarbon reservoirs.

EFFECT OF NANO- AND MICROPORES IN CARBONATE RESERVOIRS

Nano- and micropores have many significant, reservoir-based effects relative to carbonate strata that are generally engineering specific, even though they have also been shown to affect acoustic velocity in carbonates (Janjuhah et al., 2019). These effects are addressed later, although a detailed discussion of each effect is beyond the scope of this nano- and micropore review.

Nano- and micropores can be the dominant pore network in some carbonate reservoirs such as chalks. In other carbonate reservoirs, they can make up small to sizable portions of the pore network, along with macropores and/or fracture pores. Nano- to micropores affect permeability of the reservoir because of their fine pore throats (pore-throat radii less than 0.5 μm), in turn affecting production rates. In calculating porosity versus permeability transforms from wireline logs, the abundance of nano- and micropores must be taken into consideration because porosity associated with nano- and micropores may not contribute to an effective pore network (Lucia, 1995; Dutton et al., 2016).

In reservoirs consisting of a mix of pore sizes, nano- and micropores can affect fluid saturations calculated by wireline-log analysis analysis (e.g., Petricola and Watfa [1995] and Lui et al.

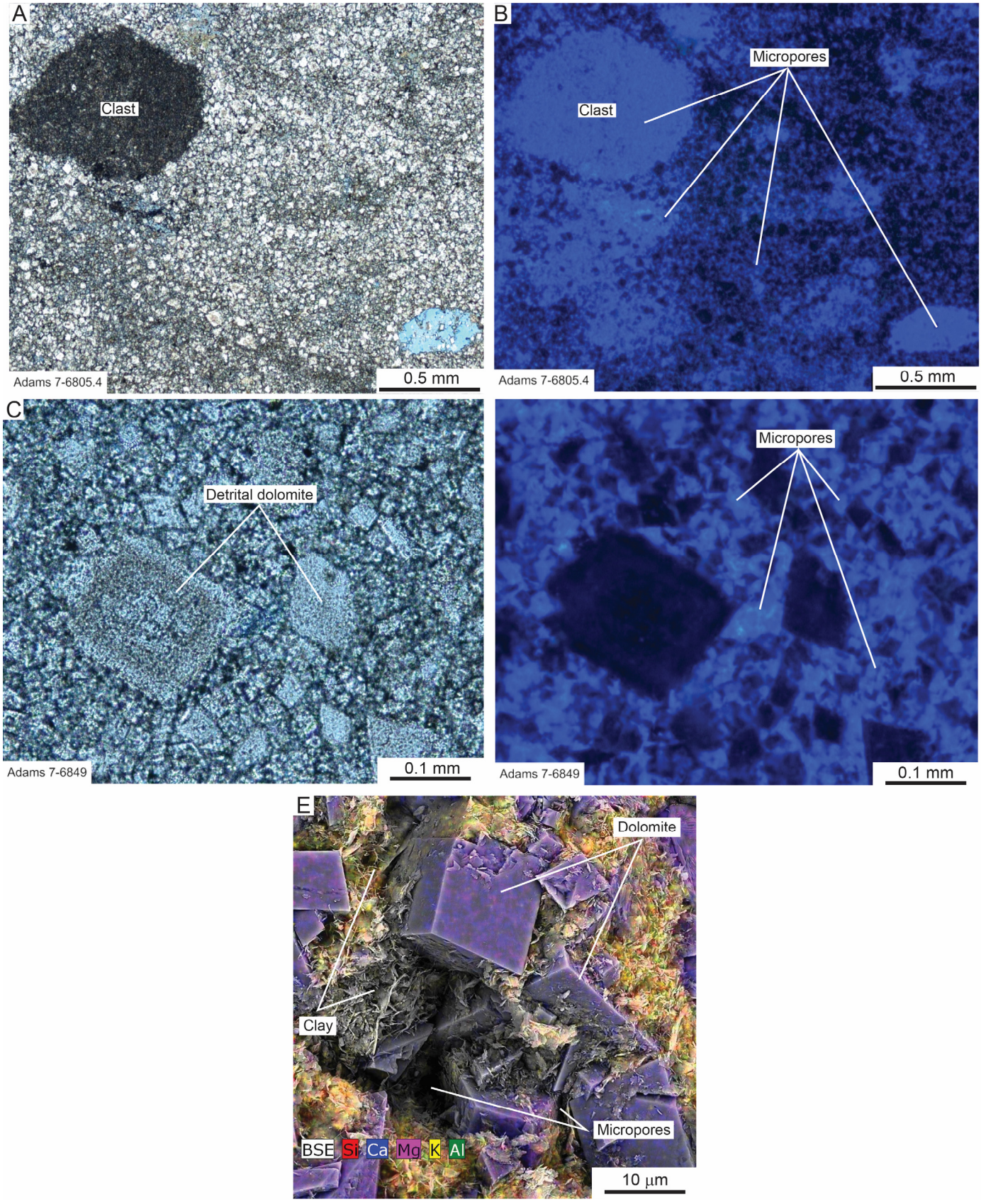

Figure 17. Inherited nano- and micropores from precursor limestone. Lower Ordovician Ellenburger Group, northern Fort Worth Basin, north-central Texas. (A) Dolowackestone with mud clasts. (B) Same as A, but photomicrograph taken under UV light. Clasts and mud are microporous, as indicated by blue haze. Pores interpreted as inherited from precursor limestone. (C) Cave-fill dolomudstone with detrital dolomite grains. (D) Same as C, but photomicrograph taken under UV light. Dolomite mud is microporous, as indicated by blue haze. Pores interpreted as inherited from precursor limestone. (E) SEM image of rock chip overlain by energy-dispersive spectroscopy element map. Sample contains abundant illite (yellow).

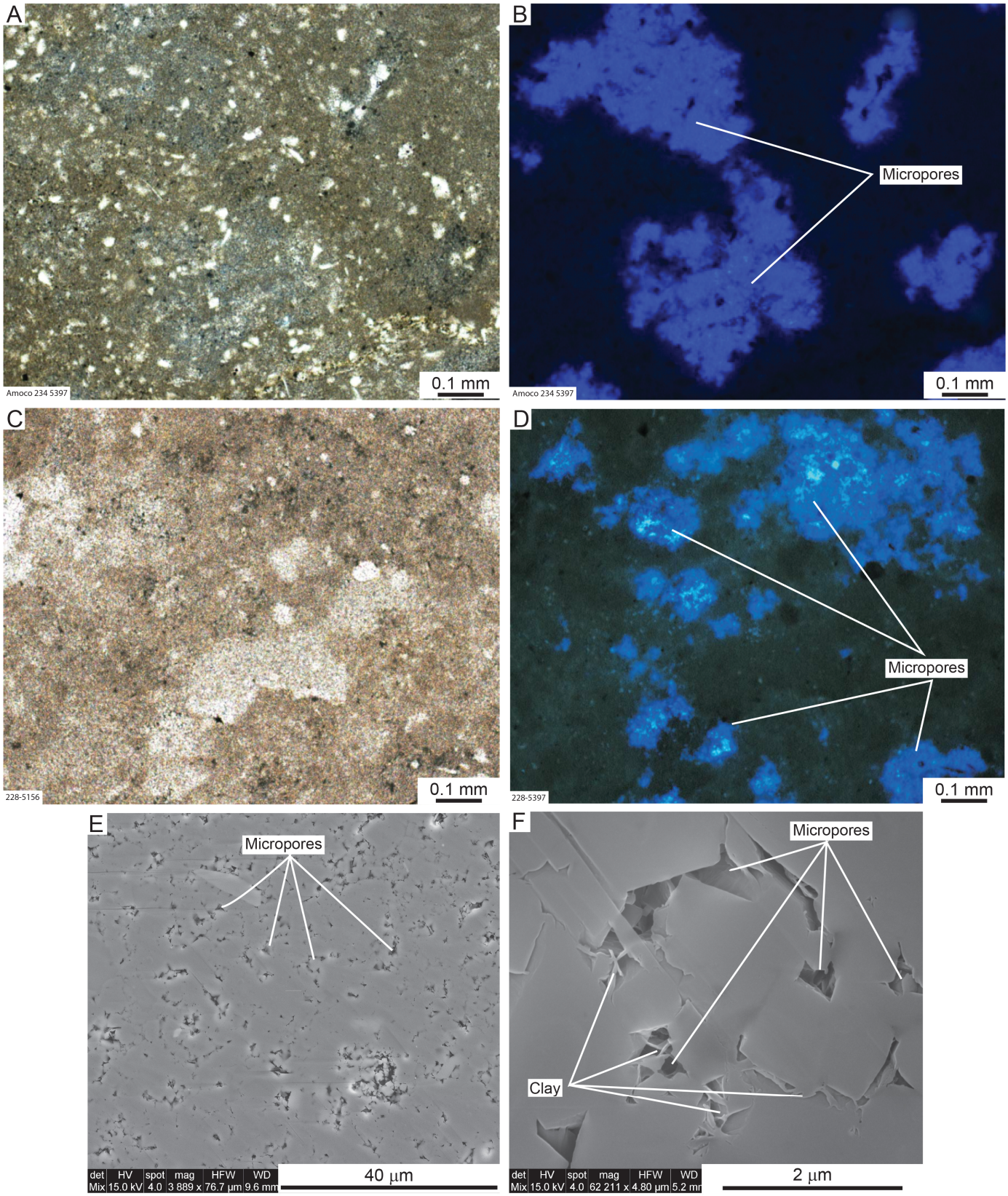

Figure 18. Inherited nano- and micropores from precursor limestone. Permian (Leonardian) Clear Fork Group, Goldsmith Field, Central Basin Platform, West Texas. (A) Silty dolomudstone. Porosity = 11.4% and permeability = 0.16 md. (B) Same as A, but photomicrograph taken under UV light. Micropores occur in patches, as shown by blue haze. Pores interpreted as inherited from precursor limestone. (C) Peloidal dolomudstone. Porosity = 11.4% and permeability = 0.16 md. (D) Same as C, but photomicrograph taken under UV light. Micropores occur in patches, as shown by blue haze. Pores interpreted as inherited from precursor limestone. (D) SEM image of Ar–ion-milled surface showing micropores between peloids. (F) SEM image of Ar–ion-milled surface showing nano- to micropores where some pores dissected by clay platelets.

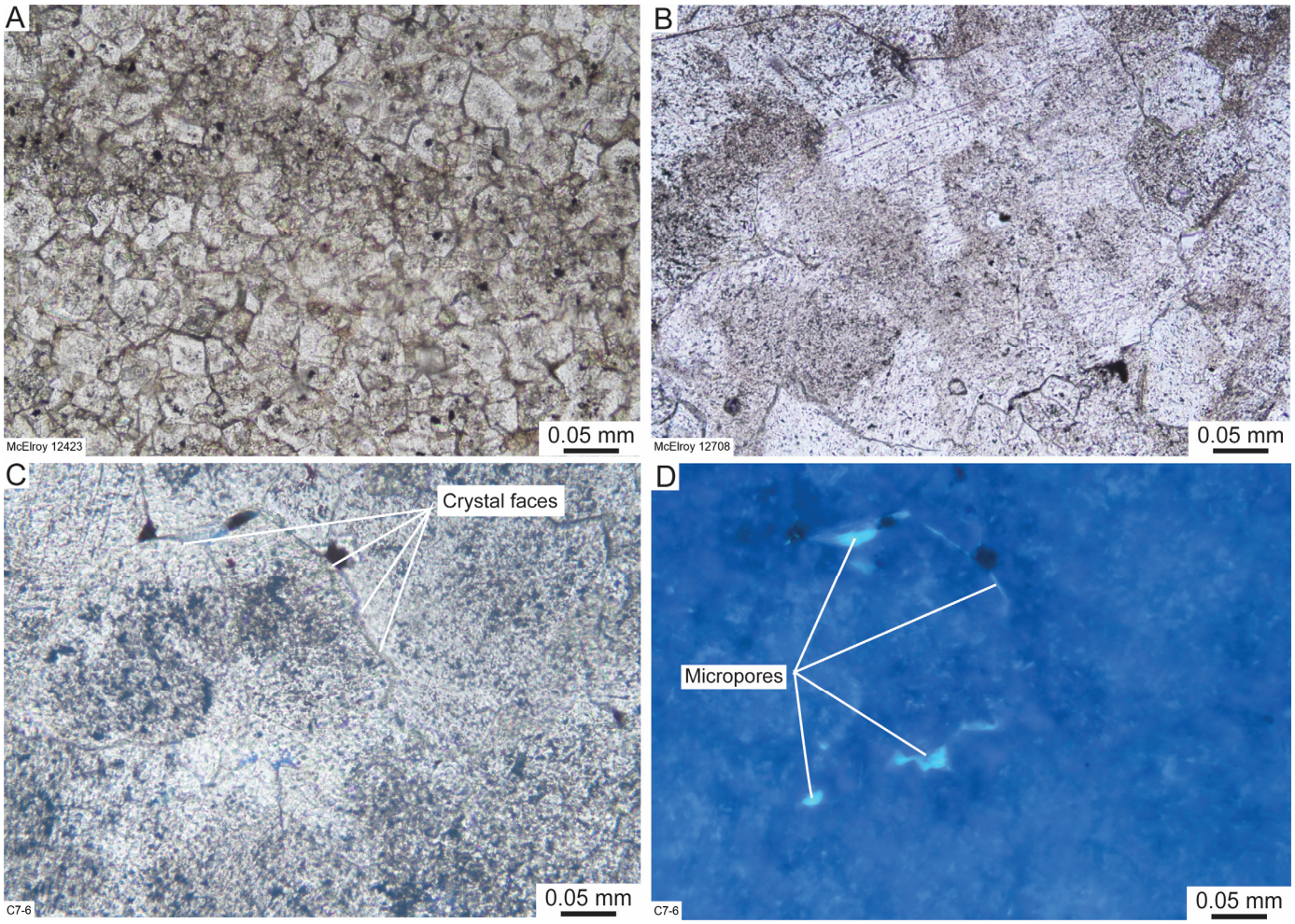

Figure 19. Whole-rock overdolomitization. Lower Ordovician Ellenburger Group, Permian Basin, West Texas. (A) Tightly-interlocking dolomite crystals resulting from overdolomitization. (B) Close-up of saddle dolomite composed of tightly-interlocking crystals. (C) Interlocking dolomite crystals with relict pores between crystals. (D) Same as C, but photomicrograph taken under UV light. Crystal-boundary nano- and micropores are shown by light-blue haze.

[2021]), which may indicate that a reservoir is water wet, even though oil may be produced during testing. Only the macropore system is produced.

Nano- and micropores in a reservoir can affect thickness of the transition-zone between hydrocarbon and water. With an increase in nano- and micropores, transition-zone thickness increases because of the higher buoyancy pressure needed to saturate the pore network (e.g., Schowalter [1979] and Lucia [1995[).

Low-permeability nano- and micropore areas will affect secondary recovery in conventional reservoirs because they will reduce sweep efficiency. This reduction, in turn, results because the oil in nano- and microporous areas may be bypassed as the reservoir is produced (e.g., Silva et al. [2012]). Also, in calculating hydrocarbon reserves in a reservoir, an overestimation of reserves may occur if the number of nonproducing nano- and micropores are taken as part of the producible volume because these nano- and micropores may not be hydrocarbon saturated and not available for production. Amount of effective porosity must be determined in order for recovery efficiency to be defined.

An important fact about nano- and micropores in limestones is that they can survive burial to greater depths (i.e., higher temperatures) than can macropores. In both sandstones and carbonates, the literature shows that megapores cement up earlier than nano- and micropores (e.g., Loucks et al. [2013] and Loucks and Dutton[2019]). Therefore, according to Loucks et al. (2013), at depths of greater than 12,000 to 13,000 ft (3700–4000 m) (depending on the thermal gradient), nano- and micropores will dominate the pore network in many limestone reservoirs. Consequently, when drilling deeper, buried-carbonate prospects in which higher temperatures prevail, nano- and micropore reservoirs are more likely to be the most common reservoir encountered.

Furthermore, Janjuhah et al. (2019) showed that nano- and micropore abundances above 50% of total porosity volume produce slower acoustic velocity in both compressional and shear (P and S) waves. Their analyses showed that composition of carbonate-pore types is important in analyzing acoustic velocity.

Nano- and micropores can also influence mechanical behavior in carbonate rocks (e.g., Zahm and Enderlin [2010] and Regnet et al. [2015]). This observation is important because it shows nano- and micropores influence both fault and fracture formation and induced hydraulic fracturing.

EXAMPLES OF RESERVOIRS CONTAINING NANO- AND MICROPORES

In this section, examples of pore networks in reservoirs containing varying numbers of nano- and micropores are presented that cover both limestone and dolomite reservoirs, as well as

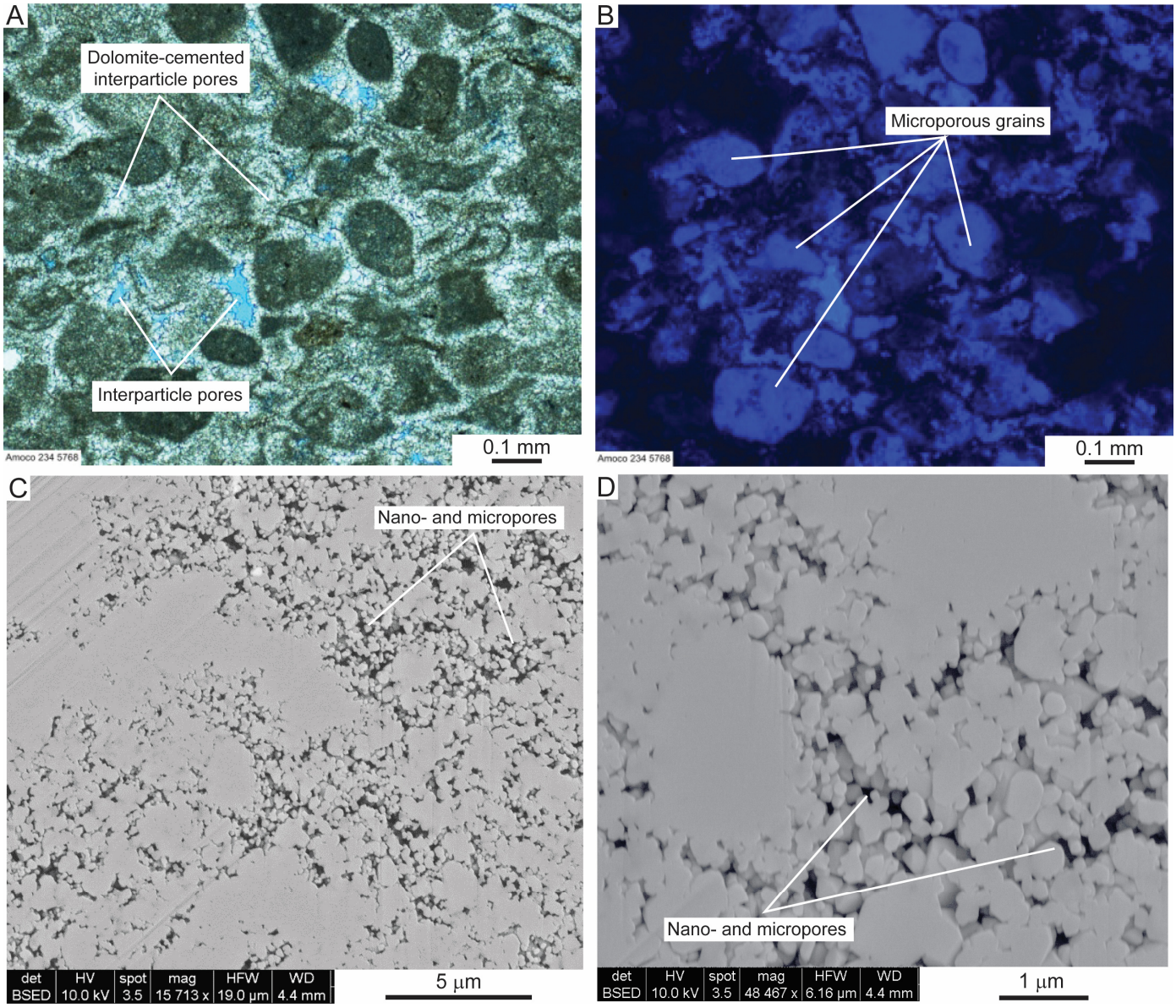

Figure 20. Differential dolomitization. Permian (Leonardian) Clear Fork Group, Goldsmith field, Central Basin Platform, West Texas. (A) Peloidal (i.e., micritized grains) dolograinstone. Interparticle pore space are partly filled with coarser dolomite cement, whereas peloids replaced by aphanitic dolomite cement resulting in differential dolomitization. (B) Same as A, but photomicrograph taken under UV light. Peloids showing abundant nano- and micropores. (C) SEM image of Ar–ion-milled surface showing dolomitization within peloids. (D) Close-up of C showing abundant nanopores.

some carbonate reservoirs in which nano- and micropores occur in solid bitumen. Also, a few examples of pulverulite reservoirs will be discussed. The case examples focus on pore networks and broader details of the geology and characteristics of the reservoirs from the literature. Thin-section photomicrographs and SEM images from these examples can reveal a wide spectrum of carbonate nano- and micropore networks.

Limestone Reservoirs

Lime-Mud-Related Reservoirs

Lower Cretaceous (Albian) Stuart City Reef Trend (Edwards), South Texas: The Stuart City Reef Trend was a shelf-margin barrier reef along the onshore northern Gulf of Mexico (Bebout and Loucks, 1974). Numerous lime packstones and grainstones formed in the backreef apron (Figs. 15 and 26), whereas rudstones and framestones constitute the reef proper. Much of the deposited backreef sediment was Mg–calcite in the form of red algae, foraminifers, and *Lithocodium*, and degradation of these allochems created abundant Mg–calcite-rich mud. As the allochems and mud chemically stabilized, they formed microrhombic calcite (Figs. 15C and 26C) and associated nano- and micropores, producing a microporous mud matrix (Figs. 15 and 26).

Lower Miocene Nido Formation Reef Complex, Offshore Palawan Area, Philippines: Off the northwest coast of the Philippines, in the northwest Palawan area, a series of large foraminifer reefs developed in the lower Miocene section that are now hydrocarbon reservoirs (Branson et al., 1977). The pore network within these reservoirs is dominated by nano- to micropores within allochems and a lime-mud matrix (Fig. 13) (based on unpublished work by the author). Larger foraminifers that com-

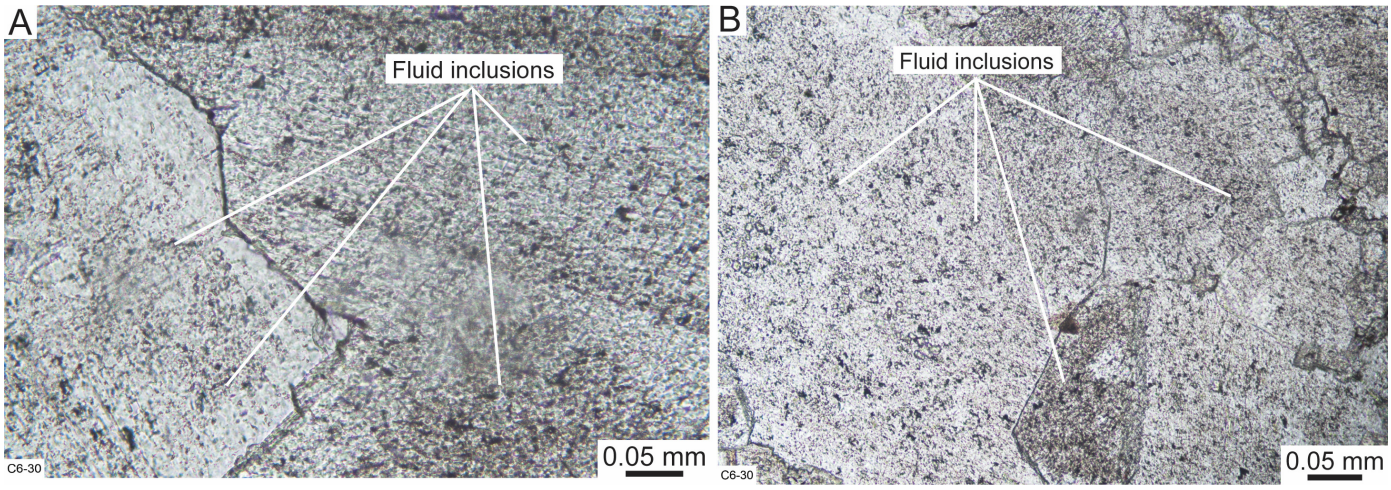

Figure 21. Fluid-inclusion pores. Lower Ordovician Ellenburger Group, Llano area, Central Texas. (A) Close-up of dolomite crystals displaying abundant fluid inclusions. (B) Another close-up of dolomite crystals displaying abundant fluid inclusions.

posed much of the reef (Fig. 13) and these foraminifers were originally Mg–calcite, which transformed into microrhombic calcite and associated micropores during diagenesis (Figs. 13B, 13D, and 13F). The mud matrix, also highly microporous (Figs. 13D and 13F), is interpreted to result from a mixture of aragonite, Mg–calcite, and calcite. Mean porosity, modest because most of the macropores are cemented by calcite (Fig. 13A), measures at 8.5% (range = 1.1–26.8%), and geometric permeability is 0.246 md (range = 0.001–276 md).

Lower Miocene Java Sea Carbonates, Indonesia: Original lime mud in the Java Sea carbonates (Fig. 27) is interpreted to have been a mixture of aragonite, Mg–calcite, and calcite on the basis of the common, poorly sorted, crystalline texture of the stabilized lime mud (Fig. 27C). A mixture of microcrystals of assorted sizes may indicate an early stage of lime-mud stabilization (Fig. 27C). On the other hand, well-sorted and well-formed crystals of microrhombic calcite may indicate a later stage of lime-mud stabilization (Fig. 27D). Ar–ion-milled SEM images of the microrhombic calcite show competitive growth between crystals (Fig. 27E and 27F), and some crystal boundaries become difficult to define. Nanopores occur between these crystal boundaries.

Chalk-Related Reservoirs

Upper Cretaceous Buda Formation, South Texas, Comanche Platform: The Upper Cretaceous Buda Formation in South Texas is a chalk deposited on the drowned Comanche Platform that is composed of highly-burrowed, calcisphere-planktic foraminifer lime wackestones and packstones with a coccolith-hash matrix (Fig. 8A) (Loucks et al., 2019). It is a fractured reservoir with some matrix contribution to production from nano- and micropores. Examples of these nano- and micropores occur in the chalk (Figs. 8A–8D). Most porosity values in the Buda chalk are less than 5%, and most permeability values are less than 0.1 md. MICP analysis provides insight into the low reservoir quality (Figs. 8E and 8F). Injection curves show high injection pressures (Fig. 8E), indicating a population of fine pore throats. Calculated pore-throat mean radii are generally less than 0.2 µm (200 nm), with several samples having pore-throat mean radii of approximately 0.005 µm (5 nm) (Fig. 8F). These fine pore-throat sizes are restrictive to two-phase flow, especially oil flow.

Upper Cretaceous (Upper Turonian to Lower Campanian) Austin Chalk, Onshore Northern Gulf of Mexico: Loucks et al. (2021) and Loucks and Peng (2021) investigated pore types and pore networks in the argillaceous Upper Cretaceous Austin Chalk along the northern onshore Gulf of Mexico. They documented that major lithofacies types ranged from well-bioturbated, slightly argillaceous chalk to well-laminated, argillaceous chalky marl (Fig. 10E). In each of the lithofacies, nano- to micropores dominate the pore network (Fig. 10), dominant pores being interparticle nanopores between coccolith hash (i.e., coccolith plates and elements) (Figs. 10A and 10B). As the concentration of clay minerals increased, more clay platelets have dissected the interparticle pores, producing finer pore throats (Fig. 10B). Mean porosity of samples is 5% (range = 0.5–8.5%), and geometric mean permeability is 121 nd (range = 3–3,375 nd) (Fig. 10E) (Loucks and Peng, 2021). Clay-poor samples have a mean porosity (6.2%) that is higher than that of the clay-rich samples (3.5%). Geometric mean permeability decreases from the clay-poor samples (351 nd) to the clay-rich samples (25 nd) (Fig. 10E).

Other nano- to micropore types present in the Austin Chalk are related to solid bitumen (Fig. 10C and D), within interparticle -pore areas. These nanopores have developed in chalks where the associated organic matter has attained R_o values higher than 0.5 to 0.6%. Three types of organic-matter-related pores are formed. The first type is spongy pores produced in solid bitumen (Figs. 10C and 10D) (Loucks et al., 2009; Ko et al., 2017b; Reed et al., 2020). These spongy pores can produce nanodarcy permeability, as well documented in the Mississippian Barnett Shale in the Fort Worth Basin in north-central Texas (Loucks et al., 2009). Another organic-matter-related pore type is modified mineral pores (Fig. 10D) (Ko et al., 2017b; Reed et al., 2020), which result when migrating bitumen and oil do not displace all the water out of a pore. When this displacement occurs, solid bitumen can be deposited on the surrounding walls, leaving a bubble in the interior where trapped water remains. A third organic-matter pore type is bubble pores (Fig. 10D), which result from thermal cracking of bitumen (Ko et al., 2017b).

Upper Cretaceous (Upper Turonian to Lower Campanian) Niobrara Formation, Western Interior Seaway: The Niobrara Formation in northwest Colorado is chalky marl with a terrigenous component consisting of 20 to 60% quartz and 5 to 15% clay minerals (Fig. 11A) (Loucks and Rowe, 2014). Throughout most of the deposition of the Niobrara chalk in this area, the environment of deposition was below storm-wave base and anoxic. In this reducing environment, bioturbation was inhibited, and delicate fecal pellets composed of coccolith hash remained intact (Fig. 11A). Within the coccolith-bearing fecal pel-

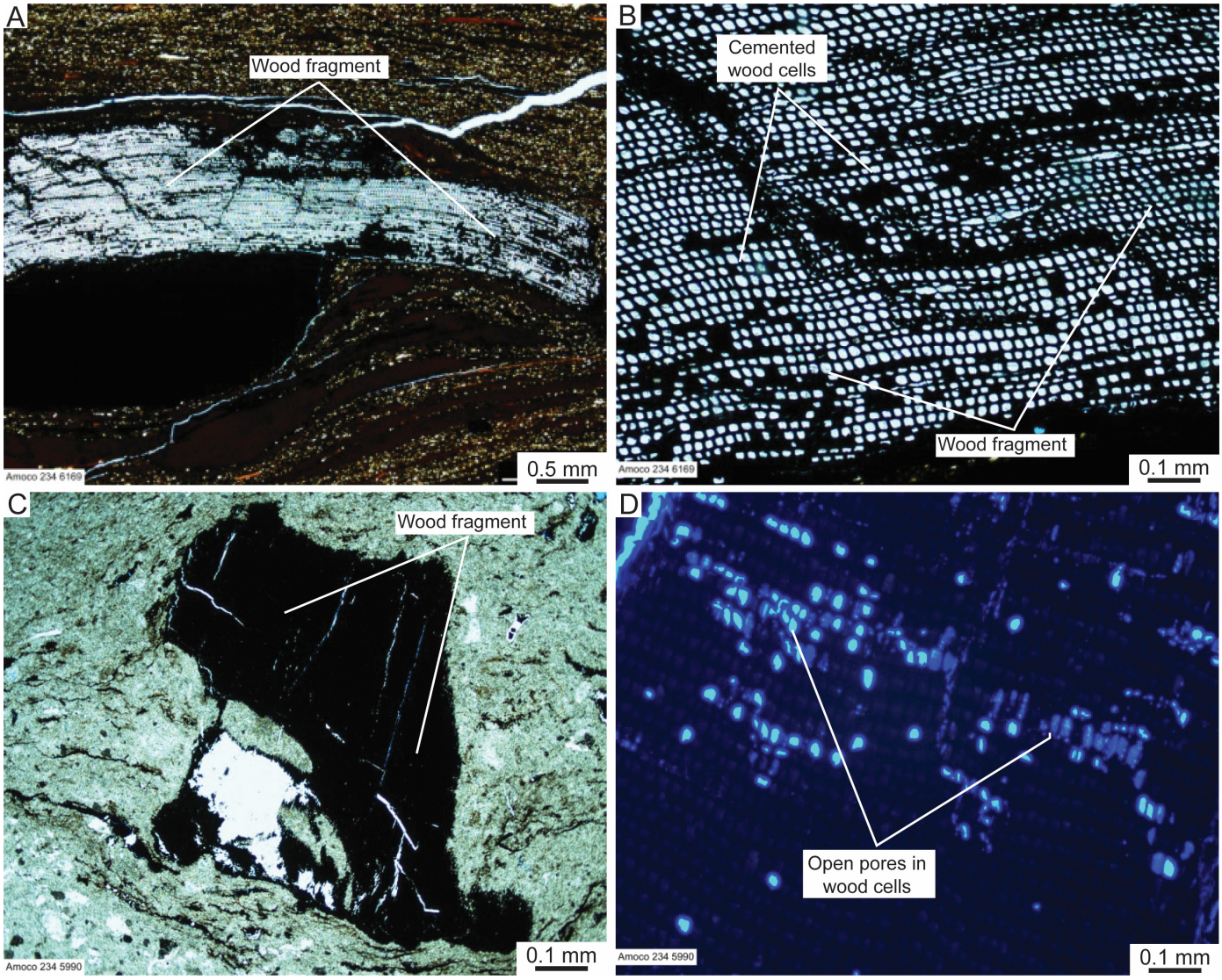

Figure 22. Nano- and micropores in type III woody kerogen. Lower Permian (Leonardian) Clear Fork Formation, Permian Basin, West Texas. (A) Fragment of wood. (B) Close-up of A showing cellular woody matter with pores filled by calcite cement. (C) Fragment of wood. (D) Close-up of C taken with UV light and cellular woody matter showing open (epoxy-filled) pores.

lets, abundant nanopores between coccolith components were preserved (Figs. 11B and 11C). Additional pores are organic-matter pores (Fig. 11D).

Upper Cretaceous (Campanian) Annona Chalk, Drowned Comanche Platform in Northwestern Louisiana: The Annona Chalk in northwestern Louisiana is a shallow (<2000 ft [<600 m] burial) oil-producing reservoir (Loucks et al., 2017). The lithology is chalk to argillaceous chalk (up to 20% quartz and 10% clay minerals) (Fig. 12). The pore network of the chalk consists of nano- to micropores between coccolith fragments (Figs. 12B–12D), with pore throats being in the nanometer range (Fig. 12F) (Loucks et al., 2017). Mean porosity is 23.8% and mean permeability is 0.42 md. MICP analysis of one sample shows a high initial injection pressure, indicating small pore throats (Fig. 12E). The nanopore throats between coccolith elements are responsible for low permeabilities, even though porosities are high and the depth of burial of the chalk is shallow.

Mg–Calcite Grains and Micrite Envelopes

Pennsylvanian (Lower Desmoinesian) Caddo Formation in North-Central Texas: The Pennsylvanian Caddo Formation in north-central Texas contains buildups of phylloid algal and *Komia* allochems (Fig. 14A) that form hydrocarbon reservoirs composed of micro- and macropores (Fig. 14) (Loucks and Fu, 2016). The extensive micropores were produced by the transformation of Mg–calcite allochems (*Komia*, fusulinids, other benthic foraminifers, ostracods, and bryozoans), micrite envelopes, microbialites, and peloidal muds to microrhombic calcite. The reservoir rock has a dual-pore system with both macropores and nano- and micropores. Porosity ranges between 0.8 and 25.1%, and permeability ranges between 0.01 and 370.5 md, reflecting this dual-pore network. MICP analysis of several Caddo samples show moderate initial injection pressures (Fig. 14E) (Loucks and Fu, 2016). A plot of pore-throat-size distribution from MICP analysis indicates a range of pore-throat-size values with many in the micropore range (Fig. 14F) (Loucks and Fu, 2016). In a dual-pore network as seen in the Caddo Formation, effects of nano- and micropores on petrophysical properties and production characteristics should be considered.

Lower Cretaceous (Albian) Stuart City Reef Trend (Edwards), South Texas Comanche Platform: The Stuart City Reef Trend was a shelf-margin barrier reef along the onshore northern Gulf of Mexico. The pore network in these carbonates,

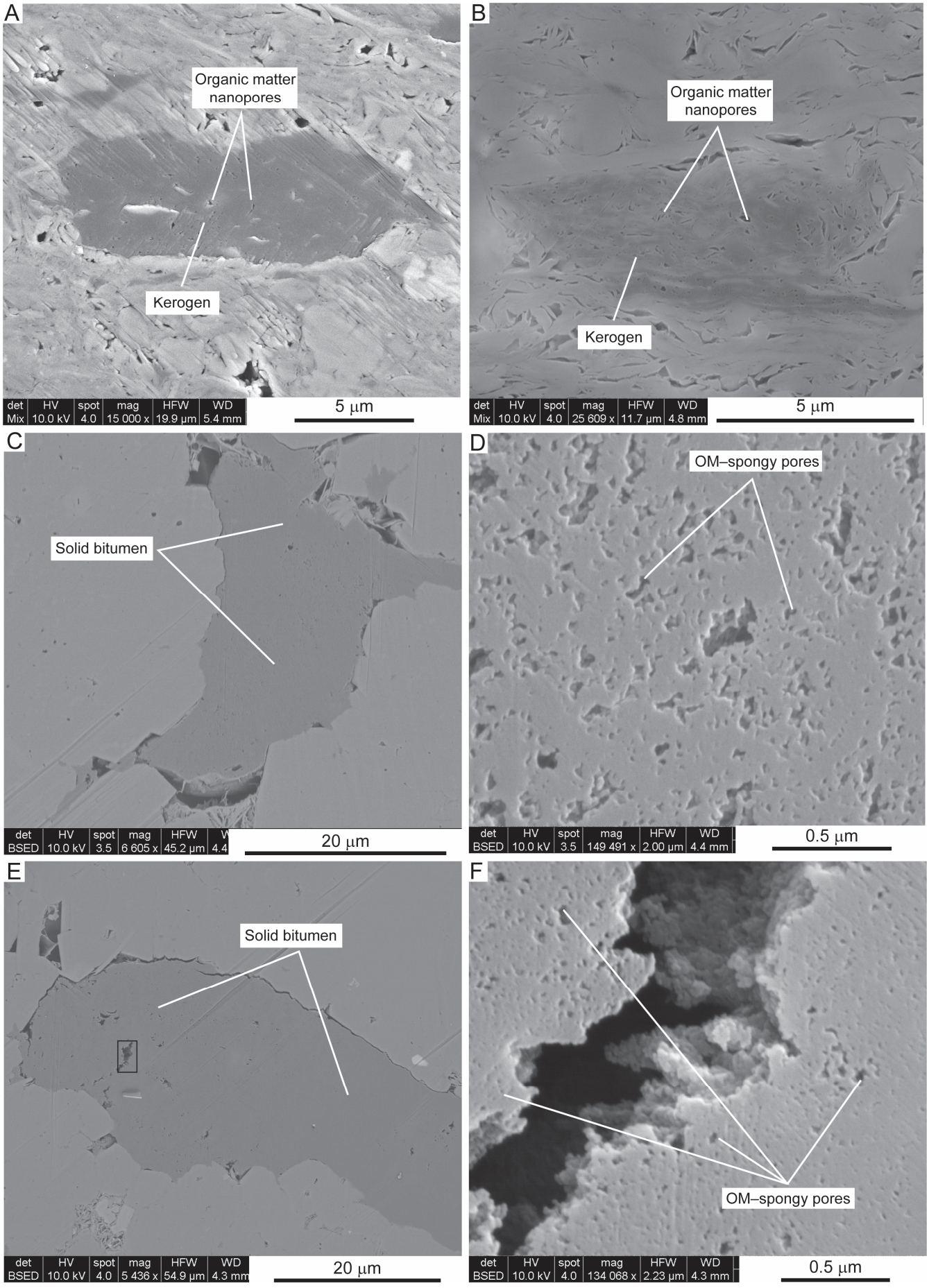
A
Organic matter nanopores
Kerogen
det HV spot mag HFW WD
Mix 10.0 kV 4.0 15 000 x 19.9 µm 5.4 mm
5 µm
B
Organic matter nanopores
Kerogen
det HV spot mag HFW WD
Mix 10.0 kV 4.0 25 609 x 11.7 µm 4.8 mm
5 µm
C
Solid bitumen
det HV spot mag HFW W
BSED 10.0 kV 3.5 6 605 x 45.2 µm 4.4
20 µm
D
OM–spongy pores
det HV spot mag HFW WD
BSED 10.0 kV 3.5 149 491 x 2.00 µm 4.4 mm
0.5 µm
E
Solid bitumen
det HV spot mag HFW WD
BSED 10.0 kV 4.0 5 436 x 54.9 µm 4.3 mm
20 µm
F
OM–spongy pores
det HV spot mag HFW WD
BSED 10.0 kV 4.0 134 068 x 2.23 µm 4.3 mm
0.5 µm

(FACING PAGE) Figure 23. Nano- and micropores in types I and II algal kerogen and solid bitumen. A and B from Eagle Ford Group in northern Central Texas and C–F from Lower Permian (Leonardian) Clear Fork Formation, Central Basin Platform, Permian Basin, West Texas. (A) Shallow-buried (254 ft [77.4 m]) type II (?) kerogen with clay flakes and original nanopores. Nanopores may be spaces between compacted kerogen grains. (B) Similar to A, showing nanopores. (C) Solid bitumen infilling megapore. (D) Close-up of C, showing spongy organic-matter pores. (E) Solid bitumen infilling megapore. (F) Close-up of E, showing spongy organic-matter pores.

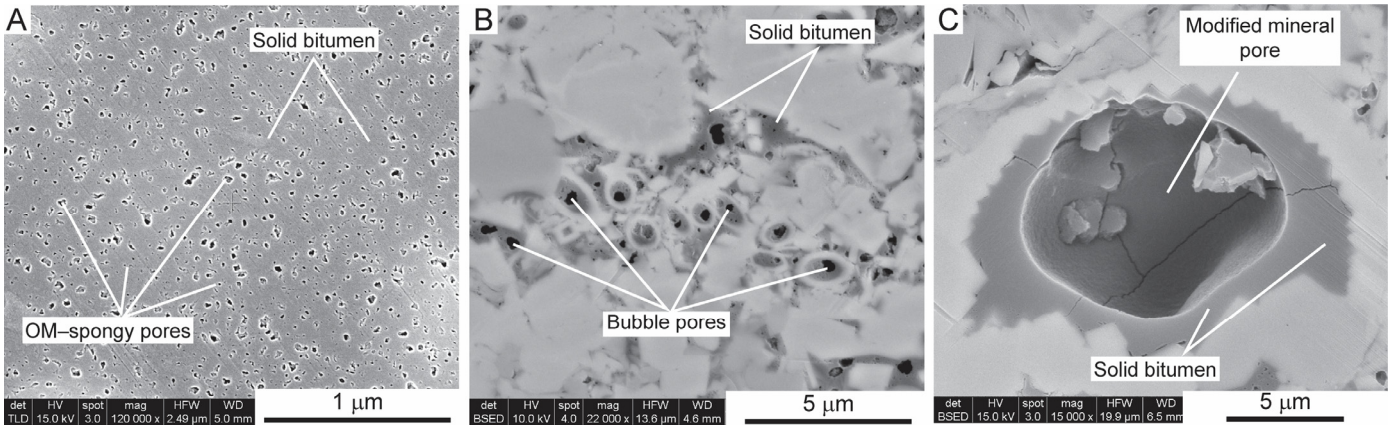

Figure 24. Nano- and micropores in solid bitumen. Upper Cretaceous (Cenomanian-Turonian) Eagle Ford Group, South Texas. (A) OM spongy pores in solid bitumen. Image from Lucy Ko. (B) OM bubble pores in solid bitumen. Image from Lucy Ko. (C) Modified mineral pore associated with solid bitumen. Image from Robert Reed.

covering over 1000 ft (305 m) of section, is dominated by nano- and micropores associated with transformed Mg–calcite allochems, micrite envelopes, and peloidal matrix (Figs. 15B, 15C, and 16E) (Loucks et al., 2013). Grains include larger foraminifers (*Dictyoconus*) (Fig. 15A), miliolids, stromatoporoids, red algae, and *Lithocodium-Bacinella* (microbialite) (Fig. 15D), which were all originally Mg–calcite. This formation is an example of a tight-gas reservoir in which macropores were cemented during burial diagenesis, and micropores, being more resistant to cementation, remain open to depths of 13,000 (~3950 m) to 15,000 ft (~4572 m). A plot of pore-throat-size distribution from MICP analysis shows a range of values, with many in the micropore-throat range (Loucks et al., 2013).

Lower Eocene El Garia Formation (Metlaoui Group), Offshore Tunisia: The middle ramp El Garia Formation is composed of bioturbated, sand- and gravel-grade, *Nummulites* packstones and grainstones (Fig. 4A). The accumulation was deposited below fair-weather wave base and above storm wave base, at a water depth estimated to be between 90 to 600 ft (~30 to 180 m) (Loucks et al., 1998). *Nummulites* tests were originally Mg–calcite that transformed to microrhombic calcite and associated micropores (Figs. 4B and 4D). Reservoir quality within El Garia *Nummulites* facies is quite variable with lime packstones and grainstones having low to high porosity (2 to 28%), and poor to good permeabilities (0.02 to 300 md) (Fig. 4F). A large amount of ineffective porosity in the El Garia Formation is caused by abundant larger intraparticle pores in Nummulites living chambers isolated by abundant nano- and micropores in test walls (Figs. 4A–4D). The microporous test walls limit connectivity between large intraparticle pores and interparticle pores.

Dolomite-Related Reservoirs

Inherited Nano- and Micropores from Precursor Limestone

Lower Ordovician Ellenburger Group, Northern Fort Worth Basin, North-Central Texas: In the Fort Worth Basin in Texas, carbonates in the Ellenburger Group that were deposited on a broad platform and upon subsequent exposure were extensively karsted (Hardage et al., 1996; McDonnell et al., 2007; Loucks, 2017). Following deposition, the section was highly dolomitized (overdolomitized), and most macropores were occluded. However, the fine-grained limestone from the host rock, host-rock lithoclasts in cave sediment fill (Figs. 17A and 17B), and cave-sediment fill (Figs. 17C–17E) that were dolomitized preserved micropores between very fine dolomite crystals (Figs. 17A, 17D, and 17E). On the basis of texture and spacing of the nano- and micropores in these fine-crystalline dolomites, the pores are thought to be inherited from the microporous limestone mud precursor (Loucks et al., 2017)

Permian (Leonardian) Clear Fork Group, Goldsmith field, Central Basin Platform, West Texas: Nano- and micropores are common in the very fine crystalline dolomites of the Clear Fork Group (Fig. 18) (Loucks and Ulrich, 2015). The nano- and micropores occur between crystals of dolomite in which dolomitization replaced an initial microporous limestone composed of Mg–calcite grains, peloids, and matrix. The nano- and micropores in the dolostones are interpreted as having several origins, one of which is that the pores are inherited from precursor lime mudstones and wackestones (Fig. 18). The nano- and microporous areas are commonly patchy (Figs. 18B and 18D).

Whole-Rock Overdolomitization

Lower Ordovician Ellenburger Group, Permian Basin, West Texas: The Ellenburger Group was deposited on a broad shallow-water shelf during Early Ordovician time in the Permian Basin (i.e., termed Tobosa Basin in Early Ordovician time) (e.g., Kerans [1988] and Loucks and Kerans [2019]). Much of the Ellenburger Group in the Permian Basin is dolomitized to an extent that the strata are completely tight, with the exception of karst and tectonic fractures and remnant nano- and micropores that are preserved at crystal boundaries (Fig. 19). These types of nano- and micropores are not abundant but occur in tight rocks at the boundaries of larger crystals (Figs. 19C and 19D).

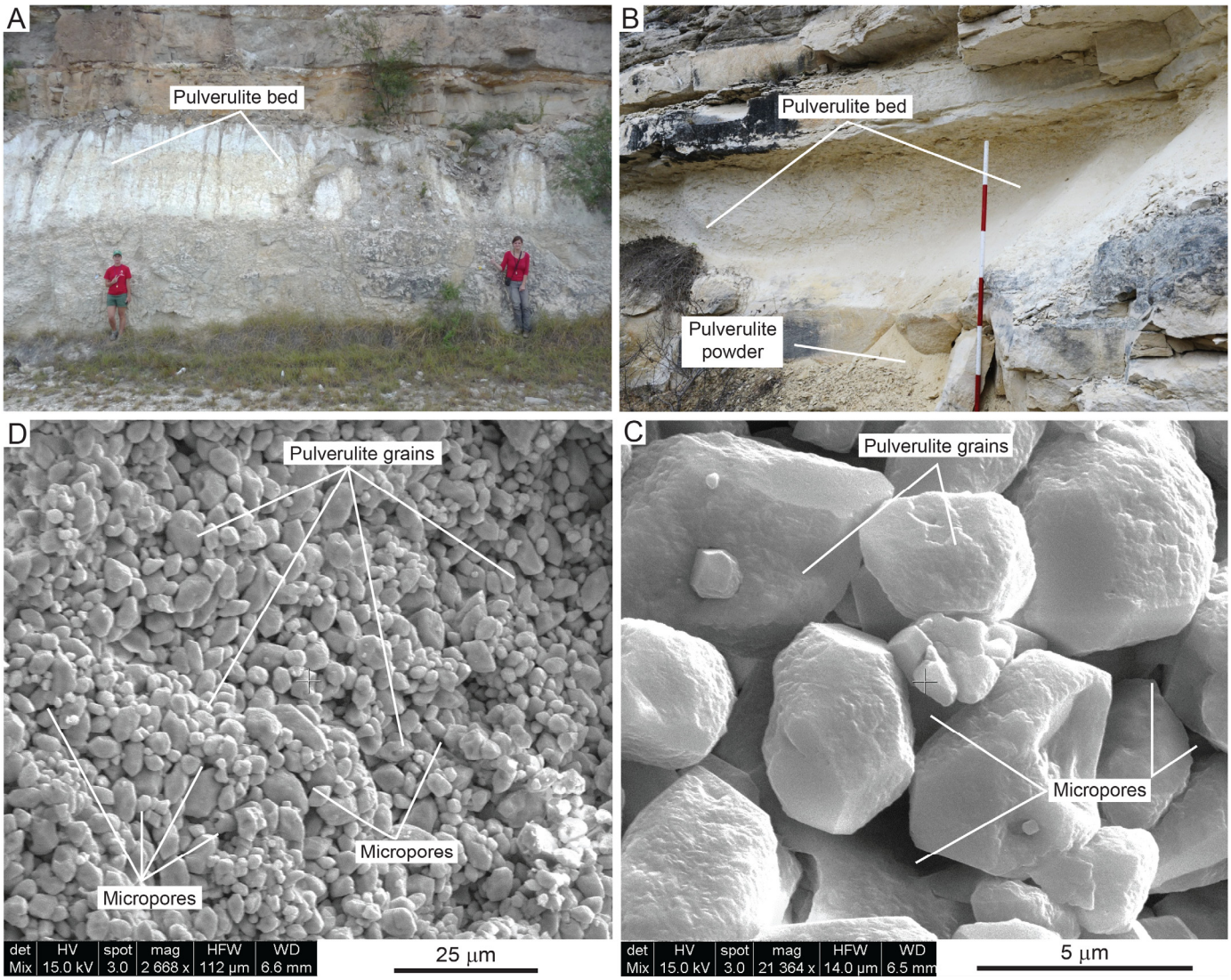

Figure 25. Nano- and micropores in pulverulite. Lower Cretaceous (Albian) Fort Terrett and Segovia formations, Central Texas. (A) In outcrop, pulverulite beds appear as light-gray to white friable units. (B) Pulverulite beds are easily eroded, commonly forming deposits of soft powder. (C) SEM image of fine grains and associated nano- and micropores in pulverulite. (D) Close-up SEM image of pulverulite grains and associated nano- and micropores.

Lower Cretaceous Kharia Formation, offshore Abu Dhabi, U.A.E.: A good example of overdolomitization in a reservoir section that resulted in a considerable decrease in porosity and permeability was documented by Yamamoto et al. (2011) in an offshore reservoir in the United Arab Emirates. In their figure 4B, a thin section of an overdolomitized grainstone is shown in which all interparticle macropores are filled with coarser, crystalline dolomite (~200 µm), and the grains have all been replaced by similar, coarser, crystalline dolomite. Unidentifiable relict grains are still visible, and the remaining pores between the dolomite crystals are in the micron range.

Differential Dolomitization at the Allochem and Matrix Scale

Permian (Leonardian) Clear Fork Group, Goldsmith Field, Central Basin Platform, West Texas: The Clear Fork Group in Goldsmith Field, West Texas, was deposited in shallow-water subtidal to supratidal environments and was heavily dolomitized, resulting in variable dolomitization patterns. One striking pattern is differential dolomitization at the grain scale, in which grains can be extensivity dolomitized, whereas pore space in between is only partly dolomitized (Loucks and Ulrich, 2015). An example reveals peloids (?) that were highly-dolomitized, leaving nano- and micropores, whereas megapore spaces between the peloids were only partly filled with dolomite cement and macropores remain (Fig. 20). This differential dolomitization process created an effective intercrystalline pore network in former primary-pore spaces with nano- and micropores in the grains.

Fluid Inclusions in Dolomite Crystals

Lower Ordovician Ellenburger Group, Central Texas: As observed in coarser crystalline dolomites, fluid inclusions (Fig. 21) can be abundant and can add to the total porosity volume—they are actually isolated nanopores (Fig. 21). Several examples from the Lower Ordovician Ellenburger dolomite in Central Texas probably contain brines and may be abundant enough to affect petrophysical properties, such as water saturation or resistivity (Fig. 21).

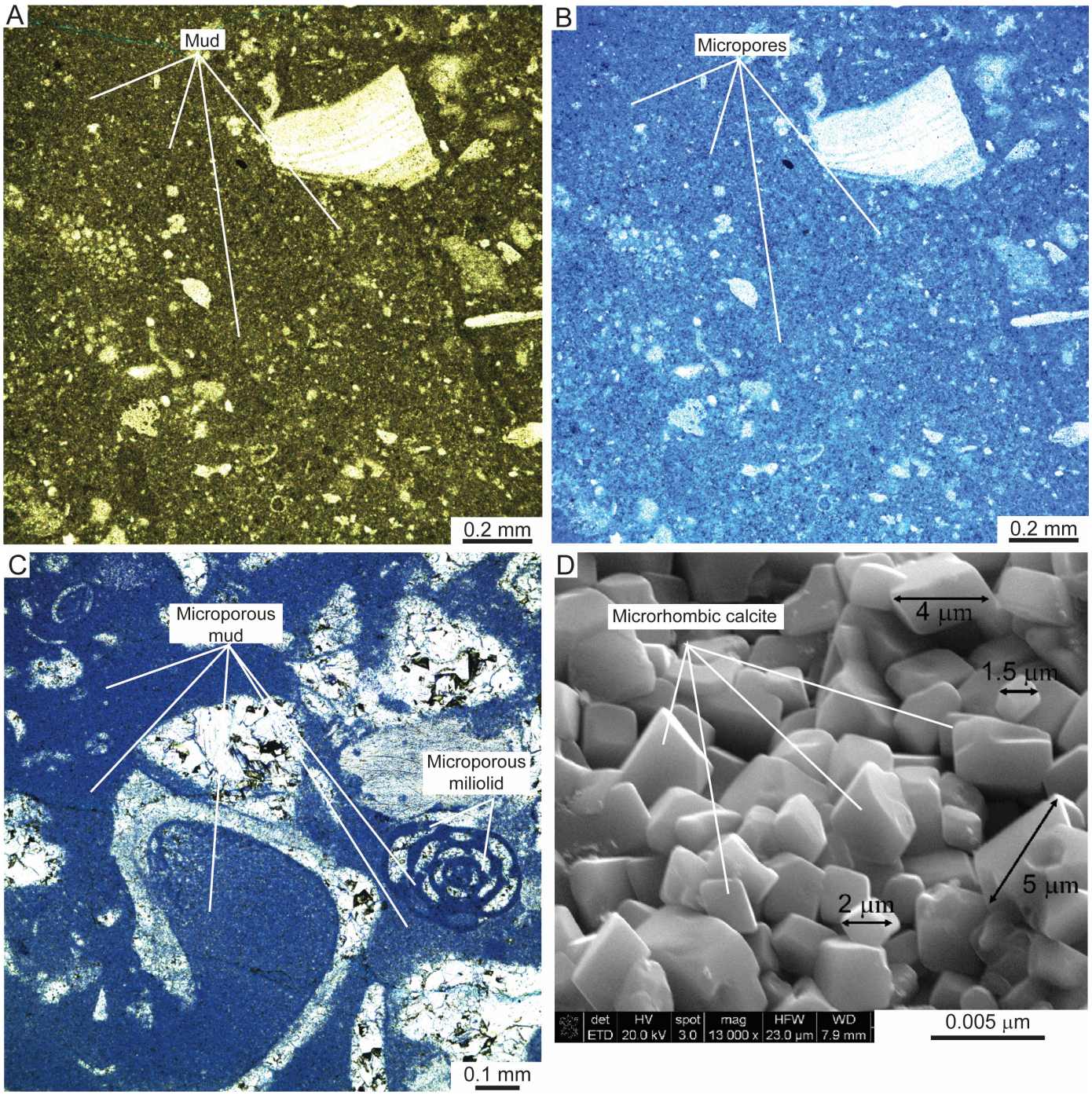

Figure 26. Microporous lime-mud matrix. Lower Cretaceous (Albian) Stuart City Reef Trend (Edwards), South Texas. (A) Microporous lime wackestone with skeletal fragments. Plain light. (B) Same as A, but photomicrograph taken under UV light. Blue haze indicates microporous areas. (C) Lime packstone photomicrograph taken under UV light. Mud matrix shows blue haze, indicating micropores. Miliolid is also microporous. (D) SEM image of rock chip showing mud matrix composed of microrhombic calcite.

Organic-Matter Pores in Carbonates

Lower Permian (Leonardian) Clear Fork Formation, Central Basin Platform, Permian Basin, West Texas

The Clear Fork Formation in Goldsmith Field on the east side of the Central Basin Platform contains examples of both woody kerogen and solid bitumen filling macropores in dolostone (Figs. 22 and 23). The Clear Fork strata in this area were deposited in environments ranging from on-shelf, deeper water, fusulinid packstones to peritidal mudstones to packstones.

Examples of woody kerogen are presented in Figure 22, and original micropores in the wood are occluded with calcite (Figs. 22A and 22B), although some woody kerogen shows that micropores can be open (Figs. 21C and 12D). In kerogen samples within larger carbonate pores, solid bitumen that formed through

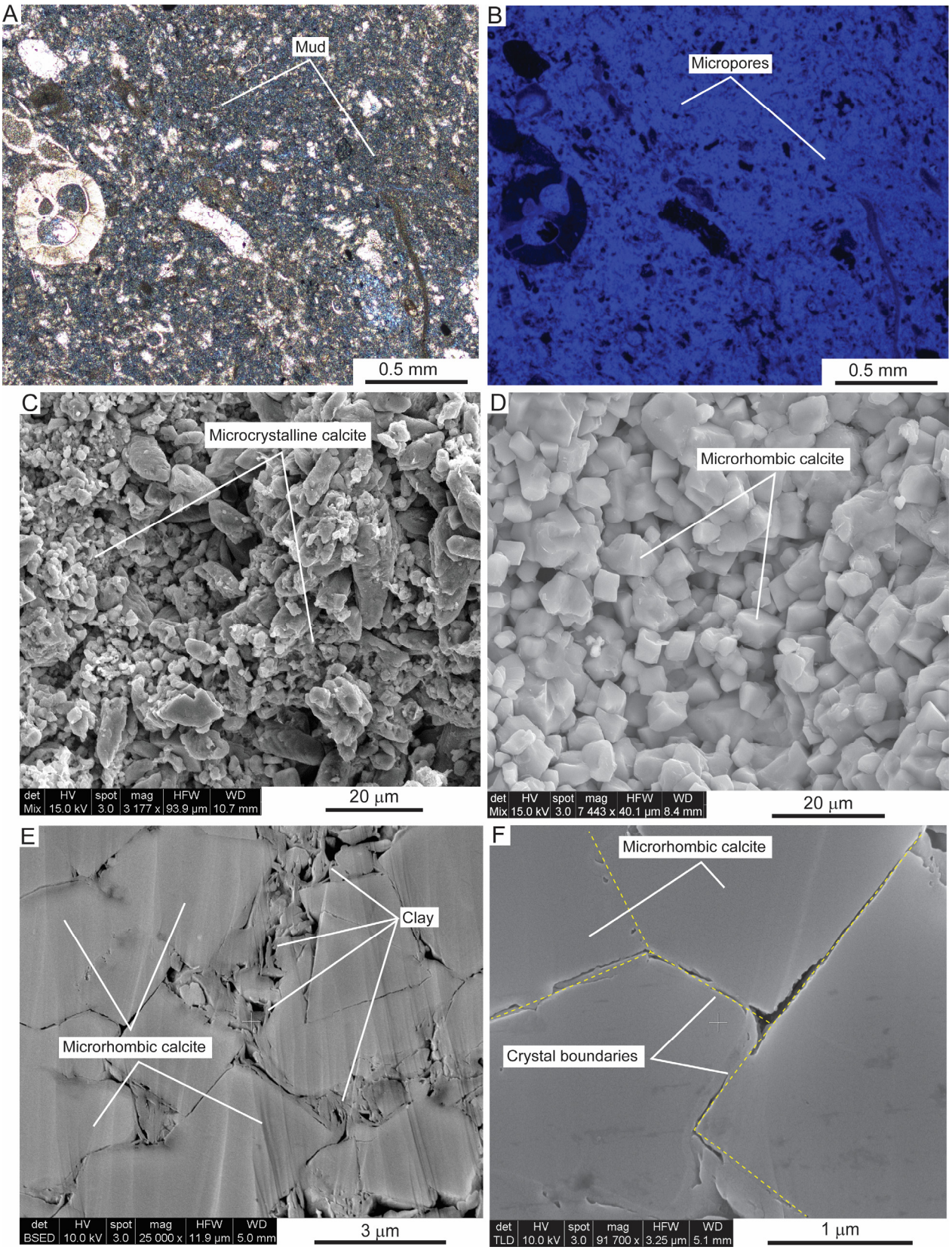

Figure 27. Microporous lime-mud matrix. Lower Miocene Java Sea carbonates, Indonesia. (A) Thin-section photomicrograph of lime packstone. (B) Same as A, but photomicrograph taken under UV light. Lime-mud matrix is microporous. (C) SEM rock-chip image, showing poorly crystalline calcite with some elongated grains. May be early stage of lime-mud stabilization. (D) SEM image of well-sorted, microrhombic calcite replacing lime mud. May be later stage of lime-mud stabilization. (E) Ar–ion-milled SEM image of microrhombic calcite and associated micropores. Some clay-minerals occur in matrix. (F) Close-up of well-cemented microrhombic calcite indicating competitive growth. Dashed yellow lines outline crystals. Only nanopores remain between crystals.

thermal maturation displays associated organic-matter nano- and micropores (Figs. 23C and 23D).

Solid bitumen fills macropores and displays numerous irregularly shaped spongy nanopores (Figs. 23C and 23D), which are as small as 20 nm. In the Clear Fork Group, this nanopore type is uncommon because this mode of solid bitumen is uncommon; therefore, these nanopores cannot add to the effective pore network.

Upper Cretaceous (Cenomanian-Turonian) Eagle Ford Group, South Texas

The Eagle Ford Group was deposited on the Upper Cretaceous drowned Comanche Platform in South Texas, generally under deeper water, anoxic conditions (e.g., Hentz and Ruppel [2010]). A number of investigations have documented the pore network in the Eagle Group (e.g., Pommer and Milliken [2015], Ko et al. [2017b], and Reed et al. [2019]). The Eagle Ford interval is organic rich, with total organic carbon generally less than 6 wt% (Pommer and Milliken, 2015; Ko et al., 2017b; Romero et al., 2018). The pore network in this organic-rich chalk is a combination of nano- to micropores associated with coccolith hash and nano- to micropore, organic-related pores (see, for example, Pommer and Milliken [2015] and Ko et al. [2017b]). According to Pommer and Milliken (2015) and Ko et al. (2017b), because organic-matter pores contribute to effective permeability pathways, they can contribute to hydrocarbon production. Ko et al. (2017b) noted that several types of organic-matter-related pores are present. These nano- and micropore-sized organic-matter pore types include bubble pores, spongy pores, and modified mineral pores containing migrated solid bitumen (Fig. 24). Organic-matter bubble pores range from nanometer scale to tens of micrometers in diameter and are rounded to subrounded (Fig. 24B). They are interpreted to be related to bitumen cracking to oil and gas (Ko et al., 2017b). Organic-matter spongy pores generally range in size from 2.5 to 200 nm (Fig. 24A) and were interpreted by Ko et al. (2017b) to be related to gas generation at higher stages of thermal maturation. Modified mineral pores (Fig. 24C) are bubbles left in the solid bitumen by a fluid (i.e., water) not being displaced out of the pore. Eagle Ford argillaceous carbonates are an example of organic matter in a carbonate forming part of an effective pore and permeability network.

Pulverulite

Lower Cretaceous (Albian) Fort Terrett and Segovia Formations, South-Central Texas

Outcrops of the Fort Terrett and Segovia formations in south-central Texas are composed of wackestones and packstones (limestones and dolostones) that are rich in nano- and micropores (Figs. 25A and 25B) (Loucks et al., 2018). During outcrop weathering, these microporous strata underwent extensive dissolution, resulting in disaggregation of the carbonate microstructure. This dissolution produced pulverulite, which is friable porous rock (Figs. 25C and 25D) to loose powder (Loucks et al., 2018). The outcrop area is a modern analog for weathering-enhanced, highly-microporous strata (i.e., pulverulite) development at unconformities.

Ordovician Viola Formation, Fort Worth Basin, North-Central Texas

The top of the buried Viola Formation limestone in north-central Texas is highly truncated by a paleo-subaerial unconformity (unpublished work by author), wherein lies a zone of oil-saturated micropores, which is interpreted as an interval of pulverulite soil strata. The soil zone displays weathered limestone crackle breccias, detrital chert with weathered patina rind, root traces, eroded and abraded skeletal grains, and quartz-sand grains. The original lime wackestones and packstones had a microporous matrix, and weathering at the unconformity enhanced this microporous matrix (Fig. 28).

Lower Cretaceous (Berriasian-Valanginian) Habshan Formation, U.A.E.

Deville de Periere et al. (2011) described microporous reservoir limestones from the Habshan Formation in the United Arab Emirates that are located beneath a major unconformity (e.g., their figures 4F and 5F). The limestone reservoir had undergone enhanced micropore development during meteoric weathering at this surface. Occurrence of enhanced micropore development resembles the pulverulite formation documented in the Fort Terrett and Segovia formations in south-central Texas. Although origin of the micropores was not made clear in the paper, the lithofacies contain numerous large benthic foraminifers (generally initially Mg–calcite) that probably transformed to microrhombic calcite and associated micropores. Also, the lime-mud-rich lithofacies may have contributed to micropore development. Deville de Periere et al. (2011) stated that these microporous reservoirs have a mean porosity of 28% and a mean permeability of 190 md.

CONCLUSIONS

Nano- and micropores, which are common in carbonates, are important to identify and quantify because they affect petrophysical properties (e.g., reservoir-hydrocarbon-saturation calculations, effective porosity, density, sonic traveltime, etc.) and, hence, flow rates, reserves, and economics. Nano- and micropores are abundant in limestones, dolomites, and associated solid bitumen in interparticle pores of unconventional tight carbonates. Special techniques, such as SEM imaging and MICP analyses, are necessary for identifying and quantifying these pore types.

In limestones, nano- and micropores are related to both depositional and diagenetic processes, whereas in strata rich in lime mud, nano- and micropores are the result of pores inherited from precursor mud and from stabilization of aragonite and Mg–calcite grains. In chalk, nano- and micropores are mainly inherited from original coccolith-rich sediment. Primary interparticle pores between the coccolith plates are reduced by compaction and cementation during burial diagenesis. During stabilization, Mg–calcite grains and micrite envelopes undergo a transformation to microrhombic calcite, resulting in associated nano- and micropores.

Dolomitization of strata is a complex diagenetic process. Several forms of nano- and micropores are known to have resulted from inherited limestone pores diagenetically altered to dolomitization-related pores. Some pores in dolostones are inherited from precursor limestone in which dolomitization occluded only some of the original limestone pores. Not uncommonly, the dolomitization process will overdolomitize the rock, leaving only nano- and micropores present at crystal boundaries. Differential dolomitization at the grain level can create strong heterogeneity in which different pores and grains experience different dolomitization histories, leaving some areas with nano- and micropores. Also, some coarser dolomite crystals can contain a large number of fluid-inclusion nanopores that probably contain brines or hydrocarbons.

During thermal maturation, in tight-carbonate, unconventional reservoirs, migrated solid bitumen forms, creating organic-matter nano- and micropores. These organic-matter nano- and micropores can be a principal part of an effective pore system.

Where microporous strata are exposed at an unconformity, a zone of microporous pulverulite can develop. These strata are friable and commonly weather to a fine powder. Where reburied, the microporous strata can be hydrocarbon reservoirs.

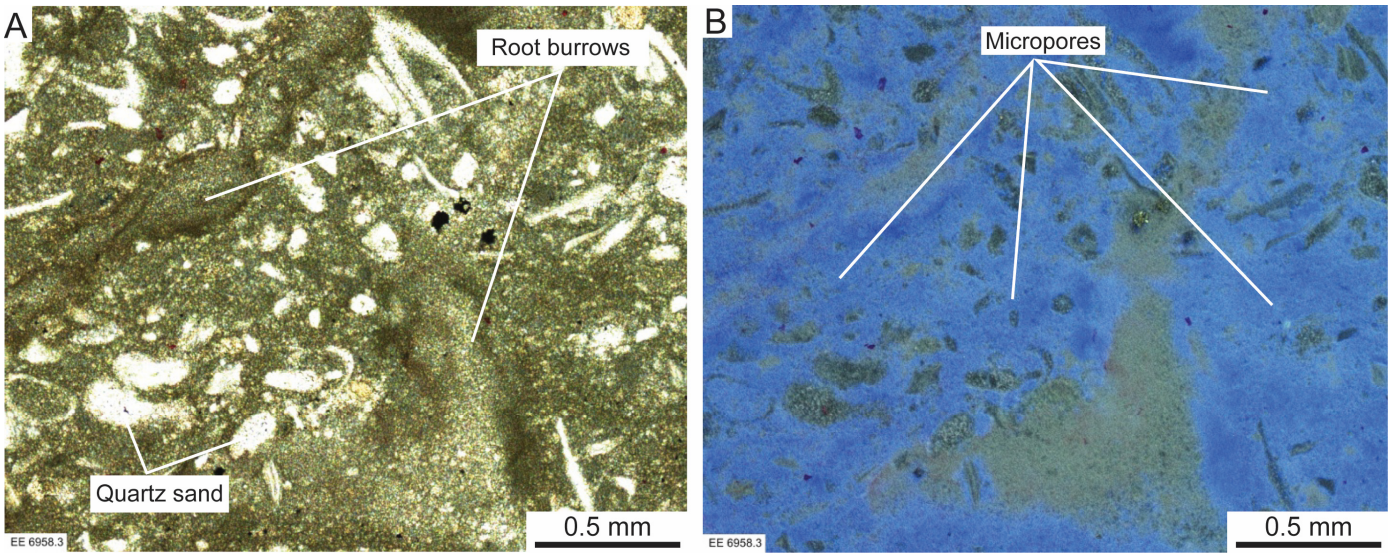

Figure 28. Nano- and micropores in paleo-pulverulite. Ordovician Viola Formation, Fort Worth Basin, north-central Texas. (A) Thin-section photomicrograph of silty lime packstone with pulverulite texture showing roots. (B) Same as A, but photomicrograph taken under UV light. Nano- and microporous areas are shown by blue haze.

This investigation and review provide an understanding of carbonate nano- and micropores and their importance in analyzing carbonate strata. In any analysis of a carbonate reservoir, an effort must be made to identify and quantify this pore type and to consider what effect it may have on reservoir properties.

ACKNOWLEDGMENTS

This review of nano- and micropores was supported by the Carbonate Reservoir Characterization Research Laboratory (RCRL) and STARR (State of Texas Advanced Resource Recovery) at the Bureau of Economic Geology, University of Texas at Austin. Discussions over the years with Jerry Lucia, Robert Handford, Alton Brown, Robert Reed, Steve Ruppel, Lucy Ko, Lowell Waite, and many others have stimulated my thinking on carbonate nano- and micropore systems. Robert Reed reviewed the initial manuscript and I appreciate the suggestions he offered. Outside reviewers include James Willis, Kim Patty, Eric Radjef, and Lowell Waite. The manuscript is much improved following their suggestions. Lucy Ko and Robert Reed provided scanning electron microscopy images of Eagle Ford organic-matter-pore networks. Lana Dieterich of the Bureau of Economic Geology edited the manuscript.

REFERENCES CITED

Alnahwi, A., and R. G. Loucks, 2019, Mineralogical composition and total organic carbon quantification using x–ray fluorescence data from the Upper Cretaceous Eagle Ford Group in southern Texas: American Association of Petroleum Geologists Bulletin, v. 103, p. 2891–2907, <https://doi.org/10.1306/04151918090>.

Arns, C. H., 2004, A comparison of pore size distributions derived by NMR and X–ray–CT techniques: Physical A: Statistical mechanics and its applications, v. 339, p. 159–165, <https://doi.org/10.1016/j.physa.2004.03.033>.

Bebout, D. G., and R. G. Loucks, 1974, Stuart City Trend, Lower Cretaceous, South Texas: Bureau of Economic Geology Report of Investigations 78, 80 p.

Benavides, F., R. Leiderman, A. Souza, G. Carneiro, and R. B. de Vasconcellos Azeredo, 2020, Pore size distribution from NMR and image based methods: a comparative study: Journal of Petroleum Science and Engineering, v. 184, Paper 106321, 11 p., <https://doi.org/10.1016/j.petrol.2019.106321>.

Bliefnick, D. M., and P. A. Mariotti, 1988, Paleoenvironmental and diagenetic reservoir characterization of the Smackover Formation Jay field, west Florida, *in* A. J. Lomando and P. M. Harris, eds., Giant oil and gas fields: Society of Economic Paleontologists and Mineralogists Core Workshop 12, p. 515–550.

Branson D. M., P. J. Newman, M. Scherer, P. J. Stalder, and R. G. Villafuerte, 1977, Hydrocarbon habitat of the NW Palawan Basin, Philippines: Indonesian Petroleum Association, Proceedings of the Petroleum Systems of SE Asia and Australasian Conference, May 1977, IPA97–OR–64, p. 815–825.

Cantrell, D. L., and E. M. Hagerty, 1999, Microporosity in Arab Formation carbonates, Saudi Arabia: GeoArabia, v. 4, p. 129–154.

Choquette, P. W., and L. C. Pray, 1970, Geologic nomenclature and classification of porosity in sedimentary carbonates: American Association of Petroleum Geology Geologists Bulletin, v. 54, p. 207–244, <https://doi.org/10.1306/5D25C98B-16C1-11D7-8645000102C1865D>.

Deville de Periere, C., M. Durlet E., Vennin, L. Lambert, R. Bourillot, B. Caline, and E. Poli, 2011, Morphometry of micrite particles in Cretaceous microporous limestones of the Middle East: Influence on reservoir properties: Marine and Petroleum Geology, v. 28, p. 1727–1750, <https://doi.org/10.1016/j.marpetgeo.2011.05.002>.

Duan, W., G. Zhiqian, F. Tailiang, M. Miaomiao, C. Yue, L. Yangbing, and Z. Chenjia, 2018, New insight into the characteristics of tight carbonate based on nuclear magnetic resonance: Energy and Fuels, v. 32, p. 2962–2972, <https://doi.org/10.1021/acs.energyfuels.7b03460>.

Dutton, S. P., W. A. Ambrose, and R. G. Loucks, 2016, Diagenetic controls on reservoir quality in deep upper Wilcox sandstones of the Rio Grande delta system, South Texas: Gulf Coast Association of Geological Societies Journal, v. 9, p. 95–110.

Eberli, G. P., G. T. Baechle, F. S. Anselmetti, and M. L. Incze, 2003. Factors controlling elastic properties in carbonate sediments and rocks: The Leading Edge, v. 22, p. 654–660.

Enos, P., and L. H. Sawatsky, 1981, Pore networks in Holocene carbonate sediments: Journal of Sedimentary Research, v. 51, p. 961–985, <https://doi.org/10.1306/212F7DF1-2B24-11D7-8648000102C1865D>.

Fabricius, I. L., and M. K. Borre, 2007, Stylolites, porosity, depositional texture, and silicates in chalk facies sediments, Ontong Java Plateau—Gorm and Tyra fields, North Sea: Sedimentology, 54, p. 183–205, <https://doi.org/10.1111/j.1365-3091.2006.00828.x>.

Fabricius, I. L., L. Gommesen, A. Krogsboll, and D. Olsen, 2008, Chalk porosity and sonic velocity versus burial depth: Influence of fluid pressure, hydrocarbons, and mineralogy: American Association of Petroleum Geologists Bulletin, v. 92, p. 201–223, <https://doi.org/10.1306/10170707077>.

Gischler, E., S. Dietrich, D. Harris, J. M. Webster, and R. N. Ginsburg, R., 2013, A comparative study of modern carbonate mud in reefs and carbonate platforms: Mostly biogenic, some precipitated: Sedimentary Geology, v. 292, p. 36–55, <https://doi.org/10.1016/j.sedgeo.2013.04.003>.

Handford, C. R., R. G. Loucks, and S. O. Moshier, 1989, Preface to nature and origin of microrhombic calcite and associated microporosity in carbonate strata: Sedimentary Geology, v. 63, p. 187–189.

Hardage, B. A., D. L. Carr, D. E. Lancaster, J. L. Simmons, Jr., R. Y. Elphick, V. M. Pendleton, and R. A. Johns, 1996, 3–D seismic evidence of the effects of carbonate karst collapse on overlying clastic stratigraphy and reservoir compartmentalization: Geophysics, v. 61, p. 1336–1350.

Hashim, M. S., and S. E. Kaczmarek, 2019, A review of the nature and origin of limestone microporosity: Marine and Petroleum Geology, v. 107, p. 527–554, <https://doi.org/10.1016/j.marpetgeo.2019.03.037>.

Hentz, T. F., and S. C. Ruppel, 2010, Regional lithostratigraphy of the Eagle Ford Shale: Maverick Basin to East Texas Basin: Gulf Coast Association of Geological Societies Transactions, v. 60, p. 325–337.

Huang, H., R. Li, F. Xiong, H. Hu, W. Sun, Z. Jiang, L. Chen, and L. Wu, , 2020, A method to probe the pore-throat structure of tight reservoirs based on low-field NMR: Insights from a cylindrical pore model: Marine and Petroleum Geology, v. 117, 11 p., <https://doi.org/10.1016/j.marpetgeo.2020.104344>.

Janjuhah, H. T., A. Alansari, and J. A. Gámez Vintaned, 2019, Quantification of microporosity and its effect on permeability and acoustic velocity in Miocene carbonates, central Luconia, offshore Sarawak, Malaysia: Journal of Petroleum Science and Engineering, v. 175, p.108–119, <https://doi.org/10.1016/j.petrol.2018.12.035>.

Kaczmarek S. E., S. M. Fullmer, and F. J. Hasiuk, 2015, A universal classification scheme for the microcrystals that host limestone microporosity: Journal of Sedimentary Research, v. 85, p. 1197–1212, <https://doi.org/10.2110/jsr.2015.79>.

Kahle, C. F., 2012, Scanning electron microscopy of pulverulite in the Silurian Lockport Dolomite near Rocky Ridge, OH: Carbonates and evaporites, v. 27, p. 3–8, <https://doi.org/10.1007/s13146-011-0076-z>.

Kerans, C., 1988, Karst-controlled reservoir heterogeneity in Ellenburger Group carbonates of West Texas: American Association of Petroleum Geologists Bulletin, v. 72, p. 1160–1183.

Ko, L. T., R. G. Loucks, T. Zhang, S. C. Ruppel, and D. Shao, 2016, Pore and pore network evolution of Upper Cretaceous Boquillas (Eagle Ford–equivalent) mudrocks: Results from gold tube pyrolysis experiments: American Association of Petroleum Geologists Bulletin, v. 100, p.1693–1722, <https://doi.org/10.1306/04151615092>.

Ko, L., R. G. Loucks, K. Milliken, Q. Liang, Q., T. Zhang, X. Sun, X., P. C. Hackley, and S. C. Ruppel, 2017a, Controls on pore types and pore-size distribution in the Upper Triassic Yanchang Formation, Ordos Basin, China: implications for pore-evolution models of lacustrine mudrocks: Interpretation, v. 5, p. SF127–SF148, <https://doi.org/10.1190/INT-2016-0115.1>.

Ko, L. T., R. G. Loucks, S. C. Ruppel, T. Zhang, and S. Peng, 2017b, Origin and characterization of Eagle Ford pore networks in the South Texas Upper Cretaceous shelf: American Association of Petroleum Geologists Bulletin, v. 101, p. 387–418, <https://doi.org/10.1306/08051616035>.

Land, L. S., 1967, Diagenesis of skeletal carbonates: Journal of Sedimentary Research, v. 37, p. 914–930.

Liu, H, Y. Luo, Y. Meng, G. Xiao, Y. Zhao, S. Zhou, and L. Shao, 2021, Effects of pore structure on the movable oil saturation in water-driven tight oil sandstone reservoirs: Journal of Petroleum Science and Engineering, v. 207, 14 p., <https://doi.org/10.1016/j.petrol.2021.109142>.

Loucks, R. G, R. T. Moody, J. K. Bellis, and A. A. Brown, 1998, Regional depositional setting and pore network systems of the El Garia Formation (Metlaoui Group, Lower Eocene), offshore Tunisia: Geological Society, London, Special Publications, v. 132, p. 355–374.

Loucks, R. G., 2002, Controls on reservoir quality in platform-interior limestones around the Gulf of Mexico: Example from the Lower Cretaceous Pearsall Formation in South Texas: Gulf Coast Association of Geological Societies Transactions, v. 52, p. 659–672.

Loucks, R. G., R. M. Reed, S. C. Ruppel, and D. M. Jarvie, 2009, Morphology, genesis, and distribution of nanometer-scale pores in siliceous mudstones of the Mississippian Barnett Shale: Journal of Sedimentary Research, v. 79, p. 848–861, <https://doi.org/10.2110/jsr.2009.0922>.

Loucks, R. G., R. M. Reed, S. C. Ruppel, and U. Hammes, 2012, Spectrum of pore types and networks in mudrocks and a descriptive classification for matrix-related mudrock pores: American Association of Petroleum Geologists Bulletin, v. 96, p. 1071–1098, <https://doi.org/10.1306/08171111061>.

Loucks, R. G., F. J. Lucia, and L. Waite, 2013, Origin and description of the micropore network within the Lower Cretaceous Stuart City Trend tight-gas limestone reservoir in Pawnee Field: Gulf Coast Association of Geological Societies Journal, v. 2, p. 29–41.

Loucks, R. G., and R. M. Reed, 2014, Scanning-electron-microscope petrographic evidence for distinguishing organic-matter pores associated with depositional organic matter versus migrated organic matter in mudrocks: Gulf Coast Association of Geological Societies Journal, v. 3, p. 51–60.

Loucks, R. G., and H. D. Rowe, 2014, Upper Cretaceous Niobrara Chalk in Buck Peak Field, Sand Wash Basin, NW Colorado: Depositional setting, lithofacies, and nanopore network: Unconventional Resources Technology Conference Paper 1918913, 13 p.

Loucks, R. G., and M. Ulrich, 2015, Origin and characterization of the nanopore/micropore network in the Leonardian Clear Fork reservoirs in the Goldsmith Field in Ector Co., Texas: American Association of Petroleum Geologists Search and Discovery Article 51164, 27 p.

Loucks, R. G., and Q. Fu, 2016, Origin and characterization of the lithofacies and dual micropore/macropore network in Pennsylvanian (early Desmoinesian) Caddo shelf-buildup complexes, Stephens County, north-central Texas: Gulf Coast Association of Geological Societies Journal, v. 5, p. 1–24.

Loucks, R. G., 2017, A review on the multiple origins of nano- and micropores in limestones and dolostones (abs.): Society of Economic Paleontologists and Mineralogists Mountjoy Carbonate Research Conference, Austin, Texas, p. 111.

Loucks, R. G., G. Frébourg, and H. D. Rowe, 2017, Upper Cretaceous (Campanian) Ozan and Annona chalks in Caddo–Pine Island Field, northwestern Louisiana: Depositional setting, lithofacies, and nanopore/micropore network: Gulf Coast Association of Geological Societies Journal, v. 6, p. 73–91.

Loucks, R. G., Z. Poros, and H. G. Machel, 2018, Characterization, origin, and significance of carbonate pulverulite: A weathering product of microporous strata: Gulf Coast Association of Geological Societies Journal, v. 7, p. 79–92.

Loucks, R. G., and S. P. Dutton, 2019, Insights into deep, onshore Gulf of Mexico Wilcox sandstone pore networks and reservoir quality through the integration of petrographic, porosity and permeability, and mercury injection capillary pressure analyses: American Association of Geologists Bulletin, v. 103, p. 745–765, <https://doi.org/10.1306/09181817366>.

Loucks, R. G., and C. Kerans, 2019, Geologic review of the Lower Ordovician Ellenburger Group of the Permian Basin, West Texas and southeast New Mexico, *in* S. C. Ruppel, ed, Anatomy of a Paleozoic basin: The Permian Basin, USA: Bureau of Economic Geology Report of Investigations 285 / American Association of Petroleum Geologists Memoir 118, v. 1, p. 295–330.

Loucks, R. G., B. G. Gates, and C. K. Zahm, 2019, Depositional systems, lithofacies, nanopore to micropore matrix network, and

reservoir quality of the Upper Cretaceous (Cenomanian) Buda Limestone in Dimmit County, southwestern Texas: Gulf Coast Association of Geological Societies Journal, v. p. 281–300.

Loucks, R. G., T. E. Larson, C. Y.C. Zheng, C. K. Zahm, L. T. Ko, J. E. Sivil, P. Sheng, S. C. Ruppel, and W. A. Ambrose, 2020, Geologic characterization of the type cored section for the Upper Cretaceous Austin Chalk Group in southern Texas: A combination fractured and unconventional reservoir: American Association of Petroleum Geologists Bulletin, v. 104, p. 2209–2245, <https://doi.org/10.1306/04222019197>.

Loucks, R. G., and S. Peng, 2021, Matrix reservoir quality of the Upper Cretaceous Austin Chalk Group and evaluation of reservoir-quality analysis methods; northern onshore Gulf of Mexico, USA: Marine and Petroleum Geology, v. 134, 11 p., <https://doi.org/10.1016/j.marpetgeo.2021.105323>.

Loucks, R. G., R. M. Reed, L. T. Ko, C. K. Zahm, and T. E. Larson, 2021, Micropetrographic characterization of a siliciclastic-rich chalk; Upper Cretaceous Austin Chalk Group along the onshore northern Gulf of Mexico, USA: Sedimentary Geology, v. 412, 19 p., <https://doi.org/10.1016/j.sedgeo.2020.105821>.

Lucia, F. J., 1995, Rock-fabric/petrophysical classification of carbonate pore space for reservoir characterization: American Association of Petroleum Geologists Bulletin, v. 79, p. 1275–1300, <https://doi.org/10.1306/7834D4A4-1721-11D7-8645000102C1865D>.

Lucia, F. J., 2004, Origin and petrophysics of dolostone pore space, *in* C. J. R. Braithwaite, G. Rizzi, and G. Darke, eds., The geometry and petrogenesis of dolomite hydrocarbon reservoirs,: Geological Society, London, Special Publications, v. 235, p. 141–155

Lucia, F. J., and R. G. Loucks, 2013, Micropores in carbonate mud: early development and petrophysics: Gulf Coast Association of Geological Societies Journal, v. 2, p. 1–10.

Machel, H. G., 2004, Concepts and models of dolomitization: A critical reappraisal: Geological Society, London, Special Publications, v. 235, p. 7–63, <https://doi.org/10.1144/GSL.SP.2004.235.01.02>.

MacIntyre, I. G., and R. P. Reid, 1992, Comment on the origin of aragonite needle mud: a picture is worth a thousand words: Journal of Sedimentary Petrology, v. 62, p. 195–197.

McDonnell, A., R. G. Loucks, and T. Dooley. 2007, Quantifying the origin and geometry of circular sag structures in northern Fort Worth Basin, Texas: Paleocave collapse, pull-apart fault systems, or hydrothermal alteration?: American Association of Petroleum Geologists Bulletin, v. 91, p. 1295–1318, <https://doi.org/10.1306/05170706086>.

Moshier, S. O., 1989, Microporosity in micritic limestones: A review: Sedimentary Geology, v. 63, p. 191–213.

Peng, S., and R. G. Loucks, 2016, Permeability measurements in mudrocks using gas-expansion methods on plug and crushed-rock samples: Marine and Petroleum Geology, v. 73, p. 299–310, <https://doi.org/10.1016/j.marpetgeo.2016.02.025>.

Peng, S., T. Zhang, R. G. Loucks, and J. Shultz, 2017, Application of mercury injection capillary pressure to mudrocks: Conformance and compression corrections: Marine and Petroleum Geology, v. 88, p. 30–40, <https://doi.org/10.1016/j.marpetgeo.2017.08.006>.

Petricola, M. J., and M. Watfa, 1995, Effect of microporosity in carbonates: introduction of a versatile saturation equation: Society of Petroleum Engineers Paper SPE–29841, p. 607–615, <https://doi.org/10.2118/29841-MS>.

Pittman, E. D., 1971, Microporosity in carbonate rocks: American Association of Petroleum Geologists Bulletin, v. 55, p. 1873–1881, <https://doi.org/10.1306/819A3DB2-16C5-11D7-8645000102C1865D>.

Pommer, M., and K. Milliken, 2015, Pore types and pore-size distributions across thermal maturity, Eagle Ford Formation, southern Texas: American Association of Petroleum Geologists Bulletin, v. 99, p. 1713–1744, <https://https://doi.org/10.1306/03051514151.S>.

Radke, B. M., and R. L. Mathis, 1980, On the formation and occurrence of saddle dolomite: Journal of Sedimentary Research, v. 50, p. 1149–1168.

Rashid, F., P. W. J. Glover, P. Lorinczi, D. Hussein, and J. A. Lawrence, 2017, Microstructural controls on reservoir quality in tight oil carbonate reservoir rocks: Journal of Petroleum Science and Engineering, v. 156, p. 814–826, <https://doi.org/10.1016/j.petrol.2017.06.056>.

Reed, R. M., and S. C. Ruppel, 2012, Pore morphology and distribution in the Cretaceous Eagle Ford Shale, South Texas, USA: Gulf Coast Association of Geological Societies Transactions, v. 62, p. 599–603.

Reed, R. M., 2017, Organic-matter pores: New findings from lower-thermal-maturity mudrocks: Gulf Coast Association of Geological Societies Journal, v. 6, p. 99–110.

Reed, R. M., J. E. Sivil, X. Sun, and S. C. Ruppel, 2019, Heterogeneity of microscale lithology and pore systems in an Upper Cretaceous Eagle Ford Group horizontal core, South Texas, U.S.A.: Gulf Coast Association of Geological Societies Journal, v. 8, p. 22–34.

Reed, R. M., R, G. Loucks, and L. T. Ko, 2020, Scanning electron microscope petrographic differentiation among different types of pores associated with organic matter in mudrocks: Gulf Coast Association of Geological Societies Journal, v. 9, p. 17–27.

Regnet, J. B, C. David, J. Fortin, P. Robion, Y. Makhloufi, and P. Y. Collin, 2015, Influence of microporosity distribution on the mechanical behavior of oolithic carbonate rocks: Geomechanics for Energy and the Environment, v. 3, p. 11–23, <https://doi.org/10.1016/j.gete.2015.07.002>.

Reid, P. R., and I. G. Macintyre, 1998, Carbonate recrystallization in shallow marine environments: a widespread diagenetic process forming micritized grains. Journal of Sedimentary Research, v. 68, p. 928–946, <https://doi.org/10.2110/jsr.68.928>.

Roduit, N., 2008, JMicroVision: Image analysis toolbox for measuring and quantifying 1091 components of high-definition images, <https://jmicrovision.github.io/>.

Romero, M., A., T. Nguyen, and R. Philp, 2018, Organic geochemistry of the Eagle Ford Group in Texas: American Association of Petroleum Geologists Bulletin, v. 102, p. 1379–1412, <https://doi.org/10.1306/0828171614717055>.

Schlager, W., 2005, Secular oscillations in the stratigraphic record—An acute debate: Facies, v. 51, p. 12–16.

Scholle, P. A., 1977, Chalk diagenesis and its relationship to petroleum exploration: Oil from chalks, a modern miracle?: American Association of Petroleum Geologists Bulletin, v. 61, p. 982–1009.

Schowalter, T. T., 1979, Mechanics of secondary hydrocarbon migration and entrapment: American Association of Petroleum Geologists Bulletin, v. 63, p. 723–760.

Silva J. A., M. M. Smith, J. Munakata-Marr, and J. E. McCray, 2012, The effect of system variables on in situ sweep-efficiency improvements via viscosity modification: Journal of Contaminant Hydrology, v. 136, p. 117–330, <https://doi.org/10.1016/j.jconhyd.2012.05.006>.

Steinen R. P., 1978, On the diagenesis of lime mud; scanning electron microscopic observations of subsurface material from Barbados, W. I.: Journal of Sedimentary Research, v. 48 p. 1139–1148, <https://doi.org/10.1306/212F760D-2B24-11D7-8648000102C1865D>.

Tian, F., W. Wang, N. Liu, J. Jiang, C. Niu, Y. Zhang, and Y. Li, 2018, Rock-type definition and pore characterization of tight carbonate rocks based on thin sections and MICP and NMR experiments: Applied Magnetic Resonance, v. 49, p. 631–652, <https://doi.org/10.1007/s00723-018-0993-2>.

Vanorio, T., and G. Mavko, 2009, How micrite content affects the transport, seismic, and reactive properties of carbonate rocks; implications for 4D seismic (abs.): Society of Economic Geophysicists Technical Program Expanded Abstracts 2009, p. 4338, <https://doi.org/10.1190/1.3255256>.

Washburn, E. W., 1921. The dynamics of capillary flow: Physical Review, v. 17, p. 273–283.

Windland, A. D., 1968, The role of high Mg–calcite in the preservation of micrite envelopes and textural features of organic sediments: Journal of Sedimentary Research, v. 38, p. 1320–1325.

Yamamoto, K., O. Al-Zinati, G. Ottinger, E. Edwards, G. Kompanik, and M. B. Al-Ameri, 2011, Permeability characterization of a

high–K dolomitized interval: A case study from an Early Cretaceous carbonate reservoir of a giant oil field, offshore Abu Dhabi, United Arab Emirates: Society of Petroleum Engineers Paper SPE–148254, 3 p., <https://doi.org/10.2118/148254-MS>.

Yao, Y., D. Liu, Y. Che, D. Tang, S. Tang, and W. Huang, 2010, Petrophysical characterization of coals by low-field nuclear magnetic resonance (NMR): Fuel, v. 89, p. 1371–1380, <https://doi.org/10.1016/j.fuel.2009.11.005>.

Zahm, C. K., and M. Enderlin, 2010, Characterization of rock strength in Cretaceous strata along the Stuart City Trend, Texas: Gulf Coast Association of Geological Societies Transactions, v. 60, p. 693–702.